Iron conservation by reduction of metalloenzyme inventories in the marine diazotroph Crocosphaera watsonii

Citation: Saito, M. A., E. M. Bertrand, S. Dutkiewicz, V. V. Bulygin, D. M. Moran, F. M. Monteiro, M. J. Follows, F. W. Valois, and J. B. Waterbury. "Iron Conservation by Reduction of Metalloenzyme Inventories in the Marine Diazotroph Crocosphaera Watsonii." Proceedings of the National Academy of Sciences 108, no. 6 (January 19, 2011): 2184–2189.

As Published: http://dx.doi.org/ 10.1073/pnas.1006943108

Publisher: National Academy of Sciences (U.S.)

Persistent URL: http://hdl.handle.net/1721.1/97883

Version: Final published version: final published article, as it appeared in a journal, conference proceedings, or other formally published context

Iron conservation by reduction of metalloenzyme inventories in the marine diazotroph *Crocosphaera watsonii*

Mak A. Saito[a,1], Erin M. Bertrand[a], Stephanie Dutkiewicz[b], Vladimir V. Bulygin[a,2], Dawn M. Moran[a], Fanny M. Monteiro[b], Michael J. Follows[b], Frederica W. Valois[c], and John B. Waterbury[c]

[a]Marine Chemistry and Geochemistry Department and [c]Biology Department, Woods Hole Oceanographic Institution, Woods Hole, MA 02543; and [b]Earth Atmospheric and Planetary Sciences Department, Massachusetts Institute of Technology (MIT), 77 Massachusetts Avenue, Cambridge, MA 02139

Edited* by Paul G. Falkowski, Rutgers, State University of New Jersey, Brunswick, NJ, and approved November 19, 2010 (received for review May 31, 2010)

The marine nitrogen fixing microorganisms (diazotrophs) are a major source of nitrogen to open ocean ecosystems and are predicted to be limited by iron in most marine environments. Here we use global and targeted proteomic analyses on a key unicellular marine diazotroph *Crocosphaera watsonii* to reveal large scale diel changes in its proteome, including substantial variations in concentrations of iron metalloproteins involved in nitrogen fixation and photosynthesis, as well as nocturnal flavodoxin production. The daily synthesis and degradation of enzymes in coordination with their utilization results in a lowered cellular metalloenzyme inventory that requires ~40% less iron than if these enzymes were maintained throughout the diel cycle. This strategy is energetically expensive, but appears to serve as an important adaptation for confronting the iron scarcity of the open oceans. A global numerical model of ocean circulation, biogeochemistry and ecosystems suggests that *Crocosphaera*'s ability to reduce its iron-metalloenzyme inventory provides two advantages: It allows *Crocosphaera* to inhabit regions lower in iron and allows the same iron supply to support higher *Crocosphaera* biomass and nitrogen fixation than if they did not have this reduced iron requirement.

cyanobacteria | marine iron cycle | nitrogen cycle

The biological fixation of atmospheric dinitrogen into ammonia has a major impact on the extent of marine primary production (1, 2). Only a small number of bacteria are known to contribute to nitrogen fixation in open ocean environments, and they typically comprise a tiny fraction (<0.1%) of the overall microbial community (3, 4). Among these, the unicellular diazotroph *Crocosphaera watsonii* is estimated to be a significant contributor to oceanic nitrogen fixation (4–6). Whereas much of the primary productivity in the tropical and subtropical regions of the oceans is predicted to be nitrogen limited, the diazotrophs' nitrogen source, resupplied from the large atmospheric reservoir, is essentially limitless. Instead, iron is considered the critical micronutrient for marine diazotrophs due to their use of the iron-nitrogenase protein complex containing a homodimeric iron protein with a 4Fe:4S metallocluster (NifH) and a heterotetrameric molybdenum-iron protein with an 8Fe:7S P cluster and a 7 Fe and 1 Mo MoFe cofactor (NifDK, α and β subunits) (7, 8) (Table S1). Field experiments and models both predict the distribution of oceanic nitrogen fixation to be primarily constrained by the availability of iron (2, 9–11). Despite this importance of iron on marine nitrogen fixation, there is a limited understanding of how marine diazotrophs have adapted to this low iron environment (12–17).

The coexistence of oxygenic photosynthesis and nitrogen fixation metabolisms presents a unique challenge for diazotrophs due to their high iron demands and the chemical incompatibility of molecular oxygen and the nitrogenase protein complex. Previous elemental studies measuring whole cell iron content in *Crocosphaera* found increased iron during the dark period when nitrogen fixation is occurring (15). Whereas this finding was consistent with theoretical studies predicting a large iron requirement in marine diazotrophs (13, 18), it has been somewhat controversial due to the implication of a dynamic yet poorly understood diel cycle for intracellular iron. Several unicellular diazotrophs, including *Crocosphaera watsonii*, have been observed to fix nitrogen during the dark period (Fig. 1*A*), and this is widely viewed as an adaption for temporal separation of photosynthesis and nitrogen fixation to avoid the oxygen disruption of the nitrogenase complex (6, 19, 20). Global transcriptional studies have also observed large scale changes in the transcriptomes of the unicellular diazotrophs *Crocosphaera watsonii* (21), *Cyanothece* (22), *Gloeothece* (23), and a hot-spring *Synechococcus* (24) during the diel cycle, consistent with a temporal separation of photosynthesis and nitrogen fixation. Yet the possibility that diel cycling of the transcriptome or proteome might affect the iron requirement has not been previously discussed, likely because transcriptional studies provide information about gene expression rather than actual enzyme inventories, and immunological protein studies thus far, while having detected diel oscillations of the NifH subunit in *Crocosphaera* and *Gloeothece* (23, 25), are limited to a few select proteins with no global or absolute quantitative proteome studies of diazotrophs published as of yet. As a result, it has remained uncertain whether the observed diel transcriptome cycling was needed for the maintenance of a relatively consistent proteome or was in fact causing large changes in the global proteome composition during each diel cycle.

Recent advances in proteomic technologies hold promise for elucidating mechanistic connections between the biochemistry of important microbes and global biogeochemical cycles. There are two broad approaches to mass spectrometry based proteomics: global shotgun proteomic approaches that can semiquantitatively survey the relative abundance of hundreds of proteins simultaneously using spectral counting (26), and targeted approaches that use selected reaction monitoring (SRM) mass spectrometry with isotopically labeled peptide standards for absolute quantification of proteins of interest (27). Though there are several culture-based studies of marine microbes (26, 28) and field assessments of abundant proteins (29, 30), the combined application of global and targeted proteomic approaches to problems of

Author contributions: M.A.S., E.M.B., S.D., and J.B.W. designed research; M.A.S., E.M.B., S.D., V.V.B., D.M.M., F.M.M., M.J.F., F.W.V., and J.B.W. performed research; M.A.S., E.M.B., S.D., V.V.B., and D.M.M. analyzed data; and M.A.S., E.M.B., and S.D. wrote the paper.

The authors declare no conflict of interest.

*This Direct Submission article had a prearranged editor.

Freely available online through the PNAS open access option.

[1]To whom correspondence should be addressed. E-mail: msaito@whoi.edu.

[2]Deceased June 28, 2009.

This article contains supporting information online at www.pnas.org/lookup/suppl/doi:10.1073/pnas.1006943108/-/DCSupplemental.

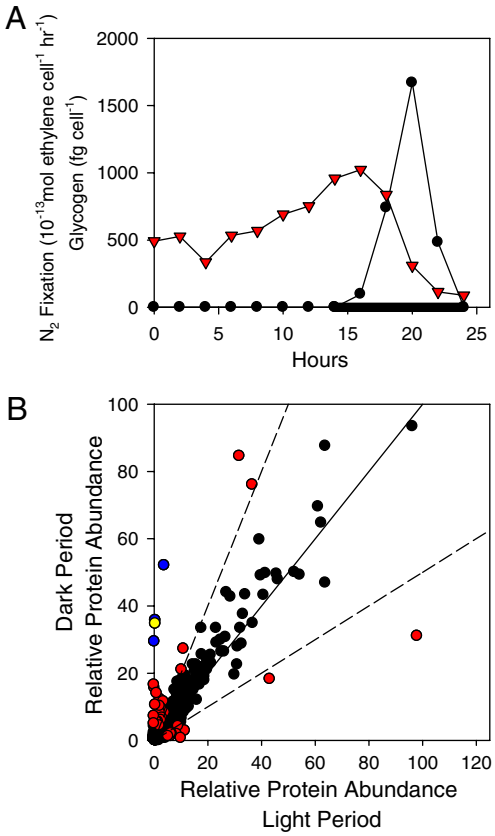

Fig. 1. Variations in the *Crocosphaera* proteome between the light and dark photoperiod. (*A*) Dark period nitrogen fixation (black) and glycogen storage (red) during a diel cycle (dark, black bar). (*B*) Relative protein abundance during light and dark periods, where similar expression (solid line, black circles; also see Fig. S1*A* for comparison of technical replicates) is contrasted by a number of proteins (colors), including the nitrogenase complex metalloenzymes (blue) and flavodoxin (yellow), with greater than 2-fold change in relative abundance (dashed lines) above a threshold of 5 normalized spectral counts in at least one treatment. Data are mean of six technical replicates.

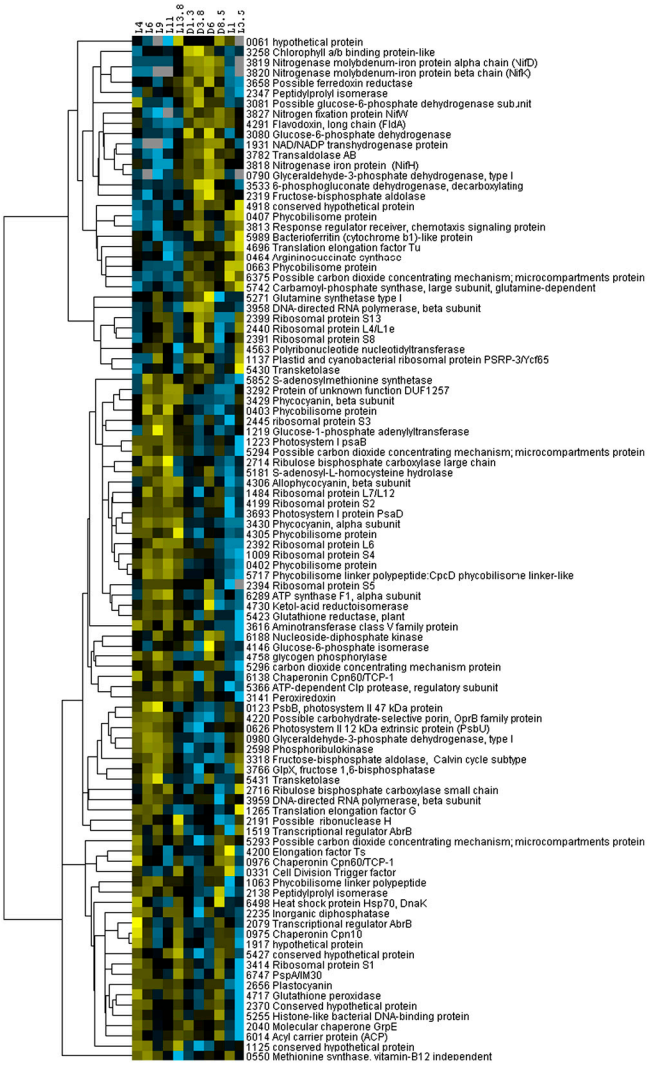

Fig. 2. Cluster analysis of global proteome during the diel cycle. Color indicates higher (yellow) or lower (blue) relative abundance relative to the centered mean value (black). Horizontal axis is hours from onset of light (L) or dark (D) period. Proteome data was filtered for proteins with at least three time points having greater than 10 spectral counts and a difference between maximum and minimum signals ≥14 spectral counts, prior to log transformation and normalization. Two major clusters were observed corresponding to the light and dark photoperiods.

marine biogeochemical relevance, such as the iron limitation of marine diazotrophy, has not yet been reported.

Results and Discussion

The diel cycle and inventory of iron metalloenzymes in *Crocosphaera watsonii* were investigated using global and targeted liquid chromatography mass spectrometry (LC-MS) proteomic techniques from three distinct culture experiments all grown on a 14 : 10 light : dark cycle: a day-night experiment sampled during the light and dark photoperiod (sampled 10 h from lights on and 7 h from lights off) analyzed for global proteome using both 1D and 2D LC-MS approaches, a time course study (diel hereon) sampled every 2–3 h for 30 h (beginning 4 h from lights on) and analyzed for global proteome using 1D LC-MS and for absolute quantities of targeted proteins, and a set of biological triplicate cultures (sampled 6.5 h into light period, and 3 and 6 h into the dark period) analyzed for targeted protein abundances by mass spectrometry.

Of the 477 unique proteins identified in the global proteomic 1D analysis of the day-night experiment [0.65% false positive rate (FPR) (31)], 37 proteins were found to have a 2-fold or greater change in abundance between the day and night (Fig. 1*B*). These results were confirmed in the deeper 2D chromatography proteome where 160 of the 1,108 identified proteins (0.11% FPR) showed a greater than 2-fold change (Fig. S1*B*). A time course of the diel cycle clearly showed a cycling of protein abundance (Fig. 2), where 100 proteins were found to be above a threshold spectral count signal (≥10) and displayed a diel variation in amplitude (max - min ≥ 14). Cluster analysis revealed two major groups that include key photosystem or nitrogen fixation proteins with increased abundances during the day and night respectively. These experiments demonstrate that the diel cycling observed in the transcriptome of unicellular diazotrophs (21, 22, 32) manifests itself in large scale changes in the global proteome, where more than 20% of the measured proteins in the diel experiment showed diel variation. In both the day-night and diel experiments, the metalloenzymes involved in nitrogen fixation in *Crocosphaera watsonii* were among those with the most pronounced changes in abundance, being largely absent during the day and present at night (Figs 1*B* and 2, Fig. S2, and Dataset S1).

Based on these global experiments, the absolute abundances of nine protein targets in the diel experiment were determined by triple quadrapole SRM mass spectrometry using isotopically labeled internal standards (Table S2). The abundance of the three nitrogenase metalloproteins ranged from nondetectable levels during the photoperiod to being among the most abundant pro-

teins in the proteome in the dark period (Fig. 3 *A–C*). At their peak abundances, the ratio of the iron protein to molybdenum-iron protein subunits (α used here) was 3.5:1, consistent with previous observations of a 3:1 cellular ratio (23) and a 2:1 stoichiometry within the nitrogenase protein complex (33). Together these global and targeted proteome measurements provide evidence for the nocturnal synthesis of the metalloenzymes in the nitrogenase complex followed by their complete diurnal degradation.

Flavodoxin was observed to increase in abundance during the dark period (Fig. 3*D*), similar to the nitrogenase metalloenzymes and in contrast with the increased flavodoxin abundances observed in most phytoplankton under iron deprivation (34). This suggests the ferredoxin-flavodoxin substitution for electron transport in photosynthesis does not occur appreciably in *Crocosphaera*. The global proteome of a short-term iron deprivation experiment was sampled during the light photoperiod to allow differentiation of iron effects from the dark expression. No increase in flavodoxin in response to iron stress was observed 24 h after the addition of an exogenous siderophore (Fig. S1 *C–F*), consistent with the hypothesis that flavodoxin could be functioning as an electron carrier for nitrogenase instead of ferredoxin (35). The use of flavodoxin at night even under iron replete conditions appears to be an adaptation for the overall minimization of the cellular iron demand in this microbe.

In a mirror image of the nitrogenase metalloenzymes and flavodoxin, numerous proteins were more abundant during the photoperiod (Figs. 1*B* and 2). In particular, several proteins from iron-rich photosystem I decreased during the dark period and increased during light period, including PsaA, PsaB, PsaD, and PsaF (PsaA and PsaB shown in Fig. 3 *E* and *F*). The iron-containing cytochromes b6 and c550 were among the most abundant cytochromes detected by spectral counting (f, P450, and b559 and c oxidase were also detected) and showed large decreases in abundance during the dark period as measured by targeted mass spectrometry (Fig. 3 *G* and *H*; 2- and 15-fold respectively). The degradation of substantial quantities of cytochrome b6 and c550 should release a number of iron-containing hemes during the dark period. Two heme oxygenases, which are capable of liberating iron from heme, were identified in the proteome, showed diel variations, and may be important in iron recycling (Fig. S2). Iron storage bacterioferritin proteins were also identified in the proteome, one of which showed some diel periodicity (Fig. S2). Diel cycling is not necessarily expected for bacterioferritin given that iron is thought to be added and removed from the ferritin cage without its degradation.

These results portray a *Crocosphaera* proteome that is dynamic, shifting its metalloenzyme inventory to suit the alternating temporal needs of nitrogen fixation and photosynthetic biochemical activity. Whereas *Crocosphaera*'s distinct nocturnal nitrogenase activity is one of its defining characteristics in both laboratory

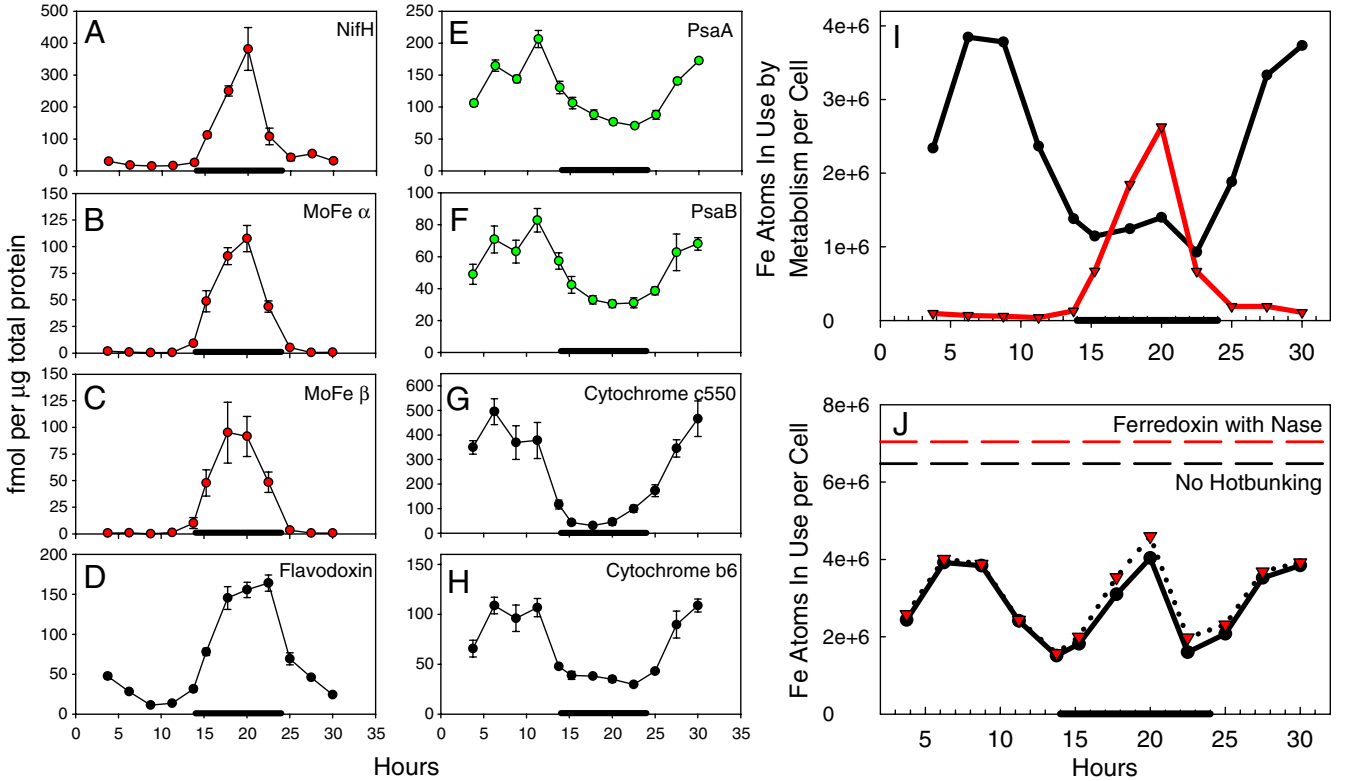

Fig. 3. Absolute quantitation of nitrogenase metalloproteins and selected photosynthesis and electron transport proteins during the diel cycle, and estimates of cellular iron stoichiometry based on absolute protein concentrations. (*A–H*) Targeted proteomic analysis of iron-nitrogenase (NifH), molybdenum-iron protein subunits (NifDK, MoFe α, MoFe β), and flavodoxin, photosystem I proteins PsaA and PsaB, and cytochromes b6 and c550 during the diel cycle (darkness, black bar) as measured using SRM triple quadrapole liquid chromatography mass spectrometry employing isotopically labeled standards. Data are mean and one standard deviation of technical triplicates. (*I*) Iron demand associated with nitrogen fixation or photosynthesis estimated from protein abundances in *A–H*, total protein and cell concentrations, and metal enyzme stoichiometries (Fig. S3 and Table S1) assuming metalloenzymes were populated with iron (darkness, black bar). (*J*) Sum of photosynthesis and nitrogenase iron estimates in two scenarios (darkness, black bar): (*i*) the *Crocosphaera* hotbunking scenario summing the calculated values in panel *I* (black circles), and (*ii*) a hypothetical nonhotbunking scenario (dashed black line), where the maximum iron required for each process [the peak of each line in panel (*I*) is summed]. Two additional scenarios are shown, where measured flavodoxin is replaced by ferredoxin, assuming a conservative 1:1 substitution (hotbunking, red triangles; nonhotbunking, dashed red line). The hotbunking scenario represents an estimated 40% savings in iron through a reduction of the iron-metalloenzyme inventory involved with nitrogenase and photosynthesis.

and field studies (6, 36), the fate of the nitrogenase protein complex during the light period has remained controversial due to the technical limitations of transcriptional and immunological methods, where transcripts do not measure protein abundance and immunological methods may not detect posttranslationally modified proteins (6, 15, 21, 36, 37). Using mass spectrometry-based analysis of multiple tryptic peptides from each protein, this study demonstrates the near complete degradation of the metalloenzymes from the nitrogenase complex and the partial degradation of certain iron-containing components of photosynthesis. The extent of proteome cycling we observed in *Crocosphaera watsonii* was surprising given the potentially significant energetic cost. This proteome cycling likely serves the dual functions of preventing oxygen disruption to the nitrogenase complex as discussed previously (6, 19), as well as providing a mechanism for a significant reduction in metabolic iron demand. We argue that the latter is true based on stoichiometric calculations from the quantitative metalloenzyme data in Fig. 3 *A–H* and the associated iron stoichiometry for each metalloenzyme (Table S1). By summing the iron associated with major metalloenzymes, we calculated the amount of iron involved in nitrogen fixation and photosynthesis throughout the diel cycle (Fig. 3*J*). By degrading these metalloenzymes when they are not in use, *Crocosphaera* reduces its iron-metalloenzyme inventory for these metabolic functions at any given time by 38%, 40%, and 75% for peak night, peak day, and minimum, respectively, compared to a hypothetical situation where these metalloenzymes are not degraded (Fig. 3*J*). An additional experiment with targeted protein analyses on biological triplicates was consistent with these estimates of iron conservation from the diel experiment, using $45 \pm 19\%$ less iron during the photoperiod (6.5 h from lights on, $n = 3$), and $38 \pm 14\%$ and $38 \pm 22\%$ less iron during the dark period (sampled at 3 h and 6 h from lights off, $n = 3$ for each). These savings in iron use would be even larger if the iron-free flavodoxin observed during the dark period (Fig. 3*D*) was replaced by iron-requiring ferredoxin (Fig. 3*J*). Iron released by the degradation of these metalloenzymes could have several fates including storage in bacterioferritin or chaperones, loss from the cell, and reuse in other metalloenzymes. Given the severe iron limiting conditions of the upper oceans (2, 9), it seems likely that a fraction of this liberated iron inventory is participating in both nitrogen fixation and photosynthesis metabolic processes. This iron conservation strategy is analogous to the maritime practice of hotbunking, referring to ships that sail with more sailors (metalloenzyme requirements) than bunks (iron atoms), where sailors on opposing shifts share the same bunk—keeping the bunks continually hot (or iron atoms in use). Whereas it is methodologically difficult to document the sharing of individual iron atoms between metabolisms, our data clearly demonstrates the reduction in iron-metalloenzyme inventory and concurrent reduction in metabolic iron demand through diel proteome cycling (Fig. 3*J*).

Iron conservation by reducing the metalloenzyme inventory likely serves as a key component of a low iron marine niche for *Crocosphaera*. *Trichodesmium* sp. is another dominant oxygenic marine diazotroph that differs from *Crocosphaera* in that it fixes both nitrogen and carbon during the photoperiod (38, 39). As a result *Trichodesmium* sp. likely does not employ this iron conservation strategy to the extent used by *Crocosphaera*. This is consistent with reports of an approximately double cellular iron to carbon stoichiometry in *Trichodesmium* compared to *Crocosphaera* (>35 and 16 ± 11 μmol Fe mol C^{-1}, respectively) (14–16), as well as estimates of a large fraction of cellular iron being necessary for nitrogen fixation (22–50%) in *Trichodesmium* (13). A previous study of cellular iron in *Crocosphaera watsonii* observed an increase in iron concentrations per cell during the dark period (15). Our calculated iron per cell attributed to nitrogen fixation and photosynthesis are roughly consistent with measured values (15), and the higher iron content at night likely results from diel proteome cycling with the added contributions of daytime uptake and accumulation of ferrous iron (21) produced by photochemical reduction (40) and photoperiod cell division (Fig. S4).

By reducing the nitrogen fixation and photosynthetic metalloenzyme inventory when each is not in use, *Crocosphaera watsonii* has evolved to require ~40% less iron than if these enzymes where maintained throughout the diel cycle (Fig. 3*J*). Though difficult to quantify, this process of resynthesizing enzymes every day must have an energetic expense. Based on our quantitative measurements, diel cycling of the three nitrogenase metalloproteins alone contributes ~2.3% of the total protein and all eight targeted proteins in Fig. 3 contribute 5.0% (using the difference between the maximum and minimum expression levels during the diel cycle). With many lower abundance proteins also undergoing diel cycling (Fig. 2), and with protein contributing roughly 40% of cellular biomass (41), these calculations provide some rough sense of the energetic cost for the increased protein synthesis required for this reduction in iron metabolic demand ("hotbunking" hereon). If *Crocosphaera watsonii* had evolved hotbunking from an ancestor that maintained its metalloenzymes through the diel, how would the trade-off between lower iron requirement and higher energetic cost affect where *Crocosphaera* would be competitive relative to its progenitor and other diazotrophs? A numerical global ocean circulation and ecosystem model (10, 42) is a useful tool to explore the implications of hotbunking on *Crocosphera's* habitat and nitrogen fixation rates in the global ocean. Our model resolves several phytoplankton types competing for resources, including analogs of several nondiazotrophs types, and unicellular and colonial marine diazotrophs, analogous to *Crocosphaera* and *Trichodesmium*, respectively. The modeled unicellular diazotrophs consist of two groups: a hypothetical control group that could not share cellular iron between photosynthesis and nitrogen fixation machinery (analogous to potential *Crocosphaera* ancestors that maintained their metalloenzyme inventory), and a hotbunking group (analogs of *Crocosphaera*, as suggested by this study) that are conferred with a lower cellular iron demand (R) at a cost to their growth rate (μ):

$$\mu_H = \alpha\mu_C, \qquad R_H = \gamma R_c \quad \text{where } \alpha,\gamma < 1.$$

The subscript H refers to hotbunkers and C refers to the non-hotbunking control group. We conducted a suite of simulations with different assumptions of the trade-off between reduced growth and iron requirement, the respective values of α and γ. A larger value of α indicates less energetic cost, and a larger value of γ indicates iron requirements closer to the control group.

Iron conservation strategies in *Crocosphaera* provided an ecological advantage in the low iron environments of the open ocean (Fig. 4 and Fig. S5). The geographical habitat of the hotbunking-analogs extended further into iron-depleted water than both the hypothetical control group and the *Trichodesmium*-analogs. In simulations with favorable combinations of trade-offs (e.g., Fig. 4), the distribution of *Crocosphaera*-analogs is broadly consistent with those suggested by observations (4, 10). These simulation results are consistent with observations suggesting that *Trichodesmium* outcompetes *Crocosphaera* in areas with high iron (43). The extent of the hotbunking unicellular diazotoph habitat is strongly regulated by the trade-off assumed (Fig. 5 and Fig. S5). Predictably, if the energetic cost is too high, hotbunking is not a desirable trait. For large cost to growth (small α) hotbunking diazotrophs do not survive (Fig. 5 *A* and *C*). On the other hand, for very little cost to growth (large α) and a high reduction in iron requirement (low γ), the hotbunking diazotrophs outcompeted the control group and expand into even more oligotrophic regions (Figs. 4*C* and 5*B* and Fig. S5 *E* and *F*). Simulations with lower requirements for iron (γ smaller) lead to a larger biomass of unicellular diazotrophs at any location than in a simulation

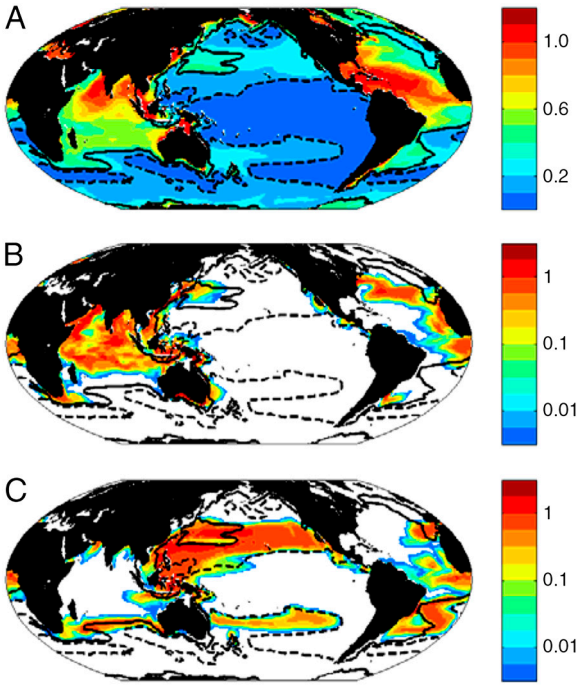

Fig. 4. Hotbunking unicellular diazotrophs inhabit waters with lower iron than the *Trichodesmium*-analogs and the unicellular control group (see Fig. S5) in the numerical simulations. Results are shown here for simulation where the hotbunking group have 90% of the growth rate and 60% the iron requirement of the control group ($\alpha = 0.9$, $\gamma = 0.6$, circle in Fig. 5). In this simulation the hotbunking diazotrophs outcompete the hypothetical control group everywhere. Annual mean model results for 0–50 m: (*A*) iron concentration (nM); (*B*) *Trichodesmium*-analogs (mgC m^{-3}); (*C*) hotbunking unicellular diazotrophs (mgC m^{-3}), analogs of *Crocosphaera watsonii*. Dashed and solid contours indicate 0.1 nM and 0.3 nM Fe respectively, and no shading (in *B* and *C*) indicates areas devoid of diazotrophs. The distribution of the diazotrophs is broadly consistent with those suggested by observations (4, 10). The model also includes analogs of several types of nondiazotrophic phytoplankton (diatoms, other large eukaryotes, *Prochlorococcus*, and other small phytoplankton). For less advantageous combinations of α and γ, the hotbunking group outcompete the control group only in the most iron-depleted regions (see Fig. 5 and Fig. S5).

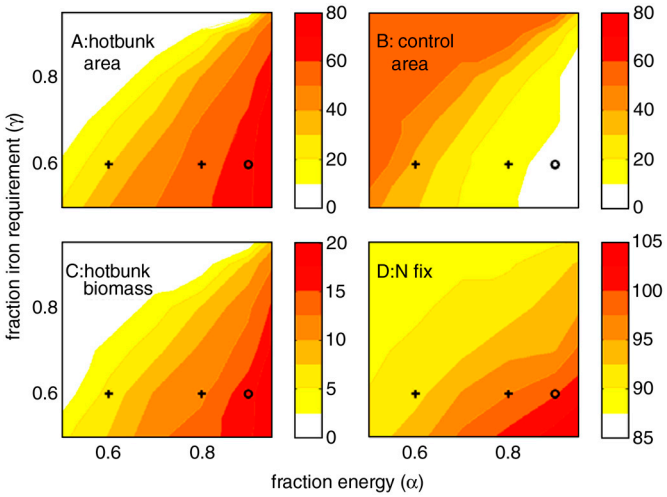

Fig. 5. Results from a series of global circulation/ecosystem model numerical simulations with different assumptions on the trade-off between reduced growth and iron requirement (values of α and γ). (*A*) Area (10^6 km^2) inhabited by hotbunking unicellular diazotrophs. (*B*) Area (10^6 km^2) inhabited by the control nonhotbunking unicellular diazotrophs. (*C*) Global abundance of hotbunking unicellular diazotrophs (TgC). (*D*) Changes in global total nitrogen fixation (TgN/y). With increased α (a smaller cost to growth) and a decreased γ (a lower requirement for iron) there are more regions where diazotrophy is supported, there is higher biomass of unicellular diazotrophs, and consequently higher total global autotrophic nitrogen fixation rates. If the energetic cost is low enough the hotbunking diazotrophs outcompete the control group everywhere (white regions of *B*). "Area" is calculated as the ocean surface area where the respective unicellular diazotrophs biomass is greater than 10^{-3} mgC m^{-3}. Nitrogen fixation rate is calculated from all three types of diazotrophs included in the simulation (hotbunking unicellular diazotrophs, control group, and *Trichodesmium*-analogs). The circle denotes parameter values used for results shown in Fig. 4 and crosses for those in Fig. S5.

with higher γ; the same iron supply could support a higher biomass. Sharing cellular iron between photosynthesis and nitrogen fixation machinery allowed the model hotbunking diazotrophs to not only expand their habitat, but also to have higher biomass per mole of available iron. These two benefits of hotbunking lead to increased global unicellular diazotroph biomass than simulations that did not include this adaptation (Fig. 5*C*). As a consequence, total global nitrogen fixation increases between simulations with α and γ combinations that shifted the population of unicellular diazotrophs from only control types to only hotbunking types (Fig. 5*D*). For the simulation shown in Fig. 4 (circles in Fig. 5) there was a 10% increase in global autotrophic nitrogen fixation relative to simulation with no hotbunkers (e.g., the white area of Fig. 5*A*). The overall affect of hotbunking on total global nitrogen fixation would be less than this value, because recent evidence demonstrates that heterotrophic nitrogen fixers also contribute significantly to marine nitrogen fixation (44).

Enzymes are agents for chemical transformations in the cycling of elements on Earth. Whereas genomic and transcriptional techniques can monitor the potential for enzyme synthesis, proteomic methods are now capable of their direct quantitation. Many require metals and hence reside at the intersection of coupled biogeochemical cycles. Our study demonstrates an application of proteomic technologies to study iron conservation in marine nitrogen fixation, where the important diazotroph *Crocosphaera* appears to have evolved a complex diel proteome cycle that results in a reduction of iron-metalloenzyme inventory. The process elucidated by the molecular-level measurements described here appears to be of global importance. With rising atmospheric CO_2 suggested to cause increases in marine nitrogen fixation (45), as well as a potential decrease in iron availability to marine phytoplankton in general (46), understanding the biochemical adaptations for iron scarcity in diazotrophs and their implications for marine primary productivity will be of increasing importance.

Methods

Axenic cultures of *Crocosphaera watsonii* were grown in SO medium (15) on a 14:10 light dark cycle. Frozen pellets were resuspended, sonicated, and centrifuged, and supernatants were solvent precipitated at −20 °C. Precipitated protein was resuspended, reduced, alkylated, and trypsin-digested. The whole cell lysate digests were analyzed using by liquid chromatography mass spectrometry (LC-MS) using a Paradigm MS4 HPLC system with reverse phase chromatography, a Michrom ADVANCE source, and a Thermo LTQ ion trap mass spectrometer. Two-dimensional chromatography involved adding an offline strong cation exchange separation using a salt gradient prior to reverse phase separation. Nine specific peptides were selected for quantitative analyses via selected reaction monitoring (SRM). Known amounts of heavy labeled versions of each peptide of interest (AQUA peptides; Sigma) were added as internal standards to *Crocosphaera* peptide extracts and analyzed using a Thermo Vantage TSQ Triple Quadrapole Mass Spectrometer with the LC and source as described for the LTQ. Peptide standard sequences and transition information are listed in Table S2. Linear Ion Trap mass spectra were processed using SEQUEST and PeptideProphet, and spectral counts were tabulated in Scaffold 2.0, with a false positive rate of less than 1% (31). Numerical simulations used the MIT general circulation model (MITgcm). The physical circulation flow fields and diffusion, constrained by observations (47), transport the organic and inorganic components of the ecosystem model. The ecosystem model was adapted from Monteiro et al. (10) and includes several types of autotrophs including several nondiazotrophs (analogs of diatoms, other large eukaryotes, *Prochlorococcus*, and other small

phytoplankton) and three types of diazotrophs (analogs of *Trichodesmium*, *Crocosphaera*, and a hypothetic control group of unicellulars that could not share cellular iron between photosynthesis and nitrogen fixation machinery). Other abundant groups of marine diazotroph groups (3) such as *Richelia* sp. symbionts found inside the diatom *Rhizosolenia* spp. and the uncultivated unicellular group A (UCYN-A) are not represented in this study due to lack of information on their iron requirements (4, 44).

ACKNOWLEDGMENTS. We acknowledge funding from US National Science Foundation Chemical and Biological Oceanography and Polar Programs (OCE-0452883, OCE-0752291, OCE-0723667, OCE-0928414, and ANT-0732665), an Environmental Protection Agency (EPA) Star Fellowship, the Woods Hole Oceanographic Institution Ocean Life Institute, the Center for Microbial Research and Education, and the Center for Environmental Bioinorganic Chemistry. This manuscript is dedicated to the memory of Vladimir Bulygin.

1. Falkowski PG (1997) Evolution of the nitrogen cycle and its influence on the biological sequestration of CO_2 in the ocean. *Nature* 387:272–274.
2. Moore JK, Doney SC, Lindsay K (2004) Upper ocean ecosystem dynamics and iron cycling in a global three-dimensional model. *Global Biogeochem Cy* 18:10.1029/2004GB002220.
3. Church MJ, Björkman KM, Karl DM, Saito MA, Zehr JP (2008) Regional distributions of nitrogen fixing bacteria in the Pacific Ocean. *Limnol Oceanogr* 53:63–77.
4. Moisander PH, et al. (2010) Unicellular cyanobacterial distributions broaded the oceanic N_2 fixation domain. *Science* 327:1512–1514.
5. Montoya JP, et al. (2004) High rates of N_2 fixation by unicellular diazotrophs in the oligotrophic Pacific Ocean. *Nature* 430:1027–1032.
6. Zehr JP, et al. (2001) Unicellular cyanobacteria fix N_2 in the subtropical North Pacific Ocean. *Nature* 412:635–638.
7. Howard JB, Rees DC (1996) Structural basis of biological nitrogen fixation. *Chem Rev* 96:2965–2982.
8. Rubio LM, Ludden PW (2008) Biosynthesis of the iron molybdenum cofactor of nitrogenase. *Annu Rev Microbiol* 62:93–111.
9. Moore CM, et al. (2009) Large-scale distribution of Atlantic nitrogen fixation controlled by iron availability. *Nat Geosci* 2:867–871.
10. Monteiro F, Follows MJ, Dutkiewicz S (2010) Distribution of diverse diverse nitrogen fixers in the global ocean. *Global Biogeochem Cy* 24:10.1029/2009GB003731.
11. Mills MM, Ridame C, Davey M, Roche JL, Geider RJ (2004) Iron and phosphorus co-limit nitrogen fixation in the eastern Tropical Atlantic. *Nature* 429:292–294.
12. Castruita M, et al. (2006) Overexpression and characterization of an iron storage and DNA-binding Dps protein from *Trichodesmium erythraeum*. *Appl Environ Microbiol* 72:2918–2924.
13. Kustka A, Sanudo-Wilhelmy S, Carpenter EJ, Capone DG, Raven JA (2003) A revised estimate of the iron use efficiency of nitrogen fixation, with special reference to the marine cyanobacterium *Trichodesmium* spp. (Cyanophyta). *J Phycol* 39:12–25.
14. Kustka A, Sanudo-Wilhelmy SA, Carpenter EJ (2003) Iron requirements for dinitrogen- and ammonium-supported growth in cultures of *Trichodesium (IMS 101)*: Comparison with nitrogen fixation rates and iron:carbon ratios of field populations. *Limnol Oceanogr* 48:1869–1884.
15. Tuit C, Waterbury J, Ravizza G (2004) Diel variation of molybdenum and iron in marine diazotrophic cyanobacteria. *Limnol Oceanogr* 49:978–990.
16. Berman-Frank I, Cullen JT, Shaked Y, Sherrell RM, Falkowski PG (2001) Iron availability, cellular iron quotas, and nitrogen fixation in *Trichodesmium*. *Limnol Oceanogr* 46:1249–1260.
17. Shi T, Sun Y, Falkowski PG (2007) Effects of iron limitation on the expression of metabolic genes in the marine cyanobacterium *Trichodesmium erythraeum* IMS101. *Environ Microbiol* 9:2945–2956.
18. Raven JA (1988) The iron and molybdenum use efficiencies of plant growth with different energy, carbon, and nitrogen sources. *Plant Phytol* 109:279–287.
19. Compaoré J, Stal LJ (2009) Oxygen and the light-dark cycle of nitrogenase activity in two unicellular cyanobacteria. *Environ Microbiol* 12:54–62.
20. Schneegurt MA, Sherman DM, Nayar S, Sherman LA (1994) Oscillating behavior of carbohydrate granule formation and dinitrogen fixation in the cyanobacterium *Cyanothece* sp. strain ATCC 51142. *J Bacteriol* 176:1586–1597.
21. Shi T, Ilikchyan I, Rabouille S, Zehr JP (2010) Genome-wide analysis of diel gene expression in the unicellular N_2-fixing cyanobacterium *Crocosphaera watsonii* WH 8501. *ISME J* 4:621–632.
22. Stockel J, et al. (2008) Global transcriptomic analysis of *Cyanothece* 51142 reveals robust diurnal oscillation of central metabolic processes. *Proc Natl Acad Sci USA* 105:6156–6161.
23. Reade JPH, Dougherty LJ, Rogers LJ, Gallon JR (1999) Synthesis and proteolytic degradation of nitrogenase in cultures of the unicellular cyanobacterium *Gloeothece* strain ATCC 27152. *Microbiology* 145:1749–1758.
24. Steunou A-S, et al. (2006) In situ analysis of nitrogen fixation and metabolic switching in unicellular thermophilic cyanobacteria inhabiting hot spring microbial mats. *Proc Nat Acad Sci USA* 103:2398–2403.
25. Mohr W, Intermaggio MP, LaRoche J (2009) Diel rhythm of nitrogen and carbon metabolism in the unicellular, diazotrophic cyanobacterium *Crocosphaera watsonii* WH8501. *Environ Microbiol* 12:412–421.
26. Xia Q, et al. (2006) Quantitative proteomics of the archaeon *Methanococcus maripaludis* validated by microarray analysis and real time PCR. *Mol Cell Proteomics* 5:868–881.
27. Malmstrom J, et al. (2009) Proteome-wide cellular protein concentrations of the human pathogen *Leptospira interrogans*. *Nature* 460:762–765.
28. Sowell SM, et al. (2008) Proteomic analysis of stationary phase in the marine bacterium *Candidatus Pelagibacter ubique*. *Appl Environ Microbiol* 74:4091–4100.
29. Ram RJ, et al. (2005) Community proteomics of a natural microbial biofilm. *Science* 308:1915–1920.
30. Sowell SM, et al. (2008) Transport functions dominate the SAR11 metaproteome at low-nutrient extremes in the Sargasso Sea. *ISME J* 3:93–105.
31. Peng J, Elias JE, Thoreen CC, Licklider LJ, Gygi SP (2003) Evaluation of multidimensional chromatography coupled with tandem mass spectrometry (LC/LC-MS/MS) for large-scale protein analysis: The yeast proteome. *J Proteome Res* 2:43–50.
32. Toepel J, Welsh E, Summerfield TC, Pakrasi HB, Sherman LA (2008) Differential transcriptional analysis of the cyanobacterium *Cyanothece* sp. strain ATCC 51142 during light-dark and continuous-light Growth. *J Bacteriol* 190:3904–3913.
33. Schindelin H, Kisker C, Schlessman JL, Howard JB, Rees DC (1997) Structure of ADP x AlF4(-)-stabilized nitrogenase complex and its implications for signal transduction. *Nature* 387:370–376.
34. Erdner DL, Anderson DM (1999) Ferredoxin and flavodoxin as biochemical indicators of iron limitation during open-ocean iron enrichment. *Limnol Oceanogr* 44:1609–1615.
35. Fillat MF, Sandmann G, Gomez-Moreno C (1988) Flavodoxin from the nitrogen-fixingcyanobacterium *Anabaena* PCC 7119. *Arch Microbiol* 150:160–164.
36. Webb EA, Ehrenreich IM, Brown SL, Valois FW, Waterbury JB (2009) Phenotypic and genotypic characterization of multiple strains of the diazotrophic cyanobacterium, *Crocosphaera watsonii*, isolated from the open ocean. *Environ Microbiol* 11:338–348.
37. Church MJ, Short CM, Jenkins BD, Karl DM, Zehr JP (2005) Temporal patterns of nitrogenase gene (nifH) expression in the oligotrophic North Pacific ocean. *Appl Environ Microbiol* 71:5362–5370.
38. Finzi-Hart JA, et al. (2009) Fixation and fate of C and N in the cyanobacterium *Trichodesmium* using nanometer-scale secondary ion mass spectrometry. *Proc Natl Acad Sci USA* 106:6345–6350.
39. Capone D, Zehr J, Paerl H, Bergman B, Carpenter E (1997) *Trichodesmium*, a globally significant marine cyanobacterium. *Science* 276:1221–1229.
40. Weber L, Volker C, Oschlies A, Burchard H (2007) Iron profiles and speciation of the upper water column at the Bermuda Atlantic time-series study site: A model based sensitivity study. *Biogeosciences* 4:689–706.
41. Rhee G-Y (1978) Effects of N:P atomic ratios and nitrate limitation on algal growth, cell composition, and nitrate uptake. *Limnol Oceanogr* 23:10–25.
42. Follows MJ, Dutkiewicz S, Grant S, Chisholm SW (2007) Emergent biogeography of microbial communities in a model ocean. *Science* 315:1843–1846.
43. Campbell J, Carpenter EJ, Montoya JP, Kustka AB, Capone DG (2005) Picoplankton community structure within and outside a *Trichodesmium* bloom in the southwestern Pacific Ocean. *Vie Milieu* 55:185–195.
44. Zehr JP, et al. (2008) Globally distributed uncultivated oceanic N_2-fixing cyanobacteria lack oxygenic photosystem II. *Science* 322:1110–1112.
45. Fu F-X, et al. (2008) Interactions between changing pCO_2, N_2 fixation, and Fe limitation in the marine unicellular cyanobacterium *Crocosphaera*. *Limnol Oceanogr* 53:2472–2484.
46. Shi D, Xu Y, Hopkinson BM, Morel FMM (2010) Effect of ocean acidification on iron availability to marine phytoplankton. *Science* 327:676–679.
47. Wunsch C, Heimbach P (2006) Estimated decadal changes in the North Atlantic meridional overturning circulation and heat flux 1993–2004. *J Phys Oceanogr* 36:2012–2024.

Supporting Information

Saito et al. 10.1073/pnas.1006943108

SI Methods

Culture Technique and Treatment. Axenic cultures of *Crocosphaera watsonii* strain WH8501 from the Waterbury laboratory culture collection were grown in nitrogen-free iron-replete SO medium (1) at 28 °C under a 14 : 10 light-dark cycle at 150 μE m^{-2} sec^{-1} in polycarbonate vessels, unless otherwise noted. All cultures were verified as axenic prior to each experiment by marine purity broth test (2) and during the experiment by examination of DNA staining microscopy slides used for cell counts (see *Microscopy and Flow Cytrometry* below). Three distinct diel experiments were conducted to obtain proteome samples. The day-night experiment consisted of discrete day and night samples collected from a 1 L culture at 10 h into the light period and 7 h into the dark period during exponential growth and analyzed for relative abundance of major proteins (1D chromatography; Fig. 1*B*) and deeper proteome comparison (2D chromatography; Fig. S1*B*). The diel experiment consisted of a 1.5 L culture grown to late log phase in a gently stirred magnetic culture vessel (Nalgene) sampled every 2–3 h over a diel cycle (under dim red light at night) for protein, microscopy (Fig. S3*A*), and flow cytometry (Fig. S3 *D*–*F*) analyses. Protein samples were analyzed for relative abundance of major proteins (1D chromatography; Fig. 2) and absolute protein abundances of selected targets (Fig. 3 *A*–*H*). A biological triplicate experiment was also conducted using 3 1 L cultures in glass furnbach flasks in midlog growth phase. Protein samples were taken 6.5 h into the light cycle and again at 3 and 6 h from onset of darkness. Two night sampling times were used to capture the transient nature of the nitrogenase expression peak. The triplicate cultures were analyzed for absolute protein abundances of selected targets, and used for an additional estimate of the overall reduction in iron-metalloenzyme inventories at each time point (see main text). An iron stress experiment was conducted with two 250 mL cultures, one with replete iron and one transferred into media with no added iron (Fig. S1 *C*–*E*). In late log phase, each culture was split into two flasks and 500 nM of the iron binding ligand desferrioxamine B (DFB, Sigma) was added to one high and one low-iron replicate. This resulted in four treatments: high iron with and without DFB and low-iron with and without DFB. In all experiments, biomass was harvested 24 h after the addition of DFB during the light period, and centrifuged at 12,400 rcf for 20 min at 4 °C, decanted and microcentrifuged at 6,700 rcf for 8 min, decanted and frozen at −80 °C.

Nitrogenase Activity and Glycogen Content. Nitrogenase activity and glycogen content were measured as previously described (3) on a separate culture experiment in 14 : 10 light-dark cycle. Briefly, nitrogen fixation was measured using acetylene-reduction assay on a Shimadzu gas chromatograph. Glycogen abundance was measured by digestion of amyloglucosidase and amylase followed by a hexokinase/glucose-6-phosphate dehydrogenase assay coupled to $NADP^+$ reduction.

Microscopy and Flow Cytometry. Cells were preserved in 0.125% final concentration ultrapure transmission electron microscopy (TEM) grade gluteraldehyde (Tousimis Research Corporation), incubated at room temperature in the dark for 15 min, flash frozen in liquid nitrogen and stored at −80 °C. 200 μL of thawed cells were collected on 0.22 μm Poretics polycarbonate filters (Osmonics Inc.) and mounted on glass slides using Vectashield hard set mounting media with DAPI (Vector Laboratories, Inc.). *Crocosphaera* cells were counted by epifluorescence microscopy and cultures were examined for bacterial contamination on a Zeiss Axioplan 2 microscope (Carl Zeiss, Inc.). For flow cytometry preserved cells were thawed, diluted with 0.22 μm filtered sterile seawater and stained with SYBR Green I fluorescent dye (Invitrogen) at a final concentration of 10×. Sodium citrate was added to the mixture at a final concentration of 10^{-5} M. A FACSCalibur flow cytometer (Becton Dickinson) was used with filtered seawater for the sheath fluid and 2.5 μm fluorescent beads for standardization (Calibrite, Becton Dickinson). Data was analyzed with WinMDI 2.8 software (J. Trotter, the Scripps Institute).

Protein Extraction and Digestion. Pellets were resupsended in cold 100 mM ammonium bicarbonate (pH 8.0, ambic hereon) and sonicated on ice with a microtip twice for 4 min on 70% duty cycle with a 5 min pause between sonication steps. Samples were centrifuged for 30 min at 6,700 rcf and 4 °C, and supernatants were precipitated overnight in 100% acetone at −20 °C, with the exception of the diel and iron experiments that were precipitated overnight in 50% acetone-50% methanol and 0.5 mM HCl at −20 °C. Precipitated protein was collected by centrifugation at 6,700 rcf for 30 min at 4 °C and dried by speed vacuum. Protein was resuspended in 0.1 mL of 6 M urea 0.1 M ambic and shaken at 400 rpm for 20 min at room temperature, then at 95 °C for 15 min. Aliquots were taken for protein determination by DC assay using bovine serum albumin as a protein standard (BioRad Inc.). Samples were reduced with 10 mM dithiothreitol (DTT) at 56 °C for 1 h, alkyated with 30 mM iodoacetamide for 1 h, and incubated with 40 mM of DTT for 1 h, prior to dilution in 1 mL ambic and digestion with trypsin for 16 h at 37 °C (1 : 50 ratio with total protein, Promega Gold Mass Spectrometry Grade, Promega Inc.). The sample was concentrated by speed vacuum for 3 h and stored at −80 °C. Aliquots for liquid chromatography mass spectrometry (LC-MS) were mixed 2 : 1 with ambic and injection volumes were adjusted to achieve equal protein loading in each experiment.

Shotgun Mass Spectrometry. The whole cell lysate digests were analyzed using a peptide Cap Trap in-line with a reversed phase Magic C18 AQ column (0.2 × 50 mm, 3 μm particle size, 200 Å pore size, Michrom Bioresources Inc.) on a Paradigm MS4 HPLC system (Michrom Bioresources Inc.) at a flow rate of 4 μL min^{-1}. A LTQ linear ion trap mass spectrometer (Thermo Scientific Inc.) was used with an ADVANCE nano-capillary electrospray source (Michrom Bioresources Inc.). The chromatography consisted of a hyperbolic gradient from 5% buffer A to 95% buffer B for 300 min, where A was 0.1% formic acid (Michrom) in water (Fisher Optima) and B was 0.1% formic acid in acetonitrile (Fisher Optima). The mass spectrometer was set to perform MS/MS on the top 7 ions using data-dependent settings and a dynamic exclusion window of 30 s. Ions were monitored over the range of 400–2000 m/z. 2D chromatography consisted of strong cation exchange (SCX) chromatography offline, followed by reverse phase chromatography of the fractions. Strong cation exchange was run on a 1 × 150 mm 5 μm particle size 200 Å pore size strong cation exchange column (Michrom Bioresources Inc.). A gradient was run from Buffer C (95% water, 5% acetonitrile, 0.1% formic acid), to filtered Buffer D (80% water, 20% acetonitrile, 0.1% formic acid, 1M NaCl) at 50 μL min^{-1}, 5 min at 2% D, ramping hyperbolically to 90% by 64 min, followed by 10 min of reequilibration at 2% D. 19–21 fractions were collected and analyzed by reverse phase chromatography using the 1D protocol described above except with a shorter 140 min gradient.

Shotgun Mass Spectra Data Processing. The 1,404,663 LTQ mass spectra collected in this study were searched using SEQUEST (Bioworks version 3.3, Thermo Inc.). An amino acid database for *Crocosphaera watsoniii* from the Joint Genome Institute Integrated Microbial Genomics server (downloaded in November 2008) was combined with a reverse sequence genome for false positive analysis for all subsequent analyses (labels with prefix CwatDraft are shortened to Cwat). The genome has not been manually annotated or closed; as a result we manually annotated the 100 most abundant proteins with diel periodicity found in Fig. 2, whereas JGI-IMG annotations were used otherwise. Database search results were further processed using the PeptideProphet statistical model (4) within Scaffold 2.0 (Proteome Software Inc.). Relative protein abundance was determined using Scaffold 2.0 for normalized spectral counting software operating on a 64-bit Ubuntu Linux workstation. Spectral counts are normalized across samples in each experiment in Scaffold, including technical replicates, to allow comparison of relative protein abundance. For the 2D experiment the spectral counts in each treatment (19 and 21 fractions each) were summed prior to normalization across samples. For the 2D day-night dataset protein identifications results from SEQUEST used filters of $\Delta CN > 0.1$, >30% ions, Xcorr vs charge state of 1.9, 2.4, and 2.9 for +1, +2, +3 charges respectively, and peptide probability <1e−3 for protein identification (Dataset S1). For all other datasets (Dataset S1), Scaffold was used for protein identifications with protein and peptide probability settings of 99.9 and 95%, respectively, with one tryptic peptide required for identification. Both approaches (SEQUEST and Scaffold) resulted in false positive rates of less than 1% (5). For cluster analysis data were log transformed, centered around the mean, and normalized with the sum of the squares equaling 1, in Cluster 3.0 (6). Analysis was performed using Kendall's tau nonparametric distance metric cluster and the dendogram was displayed using self-organizing mapping with Pearson's correlation metric (6, 7).

Targeted Mass Spectrometry. Peptides were designed as internal standards for quantitative analyses by selected reaction monitoring (SRM) using the global shotgun mass spectrometry results. Peptides were in the mass range of 800–2400 Da and lacked methionine or cysteine. SRM reactions for monitoring each peptide were selected based on successful peptide identification in the global proteomic analyses as well as those theoretically predicted by Protein Prospector MS Digest (http://prospector.ucsf.edu/prospector). Heavy isotope-labeled versions of the specific peptides (8) were obtained from Sigma-Aldrich in defined concentrations calibrated by amino acid analysis (AQUA Peptides) and handled according to the manufacturer's instructions. Heavy and native sequences of peptides, their SRMs, and collision energies are shown in Table S2. SRM analyses were performed on a Thermo Vantage TSQ Triple Quadrapole Mass Spectrometer with a Michrom Advance ion source. The SRM reactions were validated through tuning the mass spectrometer on heavy labeled reference peptides, introduced by direct infusion, to select the most abundant transitions for monitoring and to optimize the collision energies. Reverse phase chromatographic separation consisted of a peptide Cap Trap in-line with a reversed phase Magic C18 AQ column (0.2 × 50 mm, 3 mm particle size, 200 Å pore size) on a Paradigm MS4 HPLC system at a flow rate of 4 μL min^{-1} with a gradient from 5% buffer A then to 45% buffer B over 25 min and to 95% buffer B in 10 min. Buffer A and B are the same as Shotgun LC-MS analysis above. Q1 operated in 0.2 FWHM resolution and Q3 operated in 0.7 FWHM resolution. SRM reaction monitoring was scheduled based on individual peptide pair chromatographic retention times and the cycle time was 1.6 s (Table S2). Linear behavior of each peptide was validated by creating a standard curve from 1.5 to 1,650 fmol of the heavy labeled reference peptides in 1 μg *Crocosphaera* tryptic peptide sample matrix. For quantitative analysis, 150 fmols of each heavy labeled peptide was added as an internal standard to *Crocosphaera* peptide samples (1 μg protein per injection on the mass spectrometer). The amount of each target peptide of interest was calculated by ratio to the corresponding internal standard peptide abundance measured via SRM. Each biological sample was analyzed by mass spectrometry in triplicate.

Metabolic Iron Use Estimates. Absolute protein abundances were measured by targeted mass spectrometry (Fig. 3 *A–H*) and normalized to total protein extracted (Fig. S3*B*). These values were used to estimate the iron use by metabolism (Fig. 3*I*) using quantities of iron nitrogenase, molybdenum-iron β subunit, PsaA, cytochrome b6, and cytochrome c550 proteins to estimate iron involved in nitrogen fixation (former 2) and photosynthesis (latter 3) using the stoichiometries for each protein complex (Table S1). Assumptions of a 1:1:1 ratio of photosystems I, II, and ferredoxin were used here as in previous studies (9, 10), with the modification that only two iron atoms were attributed to PSII in our study (for 1 nonheme iron in PSII and 1 heme iron in cytochrome b-559), because we have direct measurements of the abundant cytochrome c550 [Fig. 3*G*; c550 can be found as part of the PSII complex and in soluble form (11)]. Because photosystem I, which we measure directly, contains far more iron that photosystem II and ferredoxin (Table S1), these assumptions should have a small effect on the calculations. Due to a potential inability to detect the dominant photosynthesis-associated ferredoxin (see *SI Results and Discussion*), the 4Fe4S stoichiometry was conservatively used. For the hypothetical situation, calculated in Fig. 3*J*, where nitrogenase substitutes ferredoxin for flavodoxin as its primary electron carrier, we used the 2Fe2S stoichiometry based on observations that a 2Fe2S ferredoxin increased slightly in abundance at night, and a conservative 1:1 stoichiometric substitution (ferredoxins are known to be more efficient than flavodoxins). Protein abundances were converted to per cell concentrations by multiplying by the measured total protein from extracted cells and dividing by the cell concentration at each time point. Whereas the measured peptide signals associated with targeted peptides appeared to be robust during the diel experiment (Fig. 3) suggesting reproducible results, we interpret these as lower estimates due to the potential for inefficiencies associated with the protein extraction. The extraction protocol was chosen for minimal processing to improve quantitative reproducibility, yet some proteins such as membrane associated proteins were likely not completely extracted. These calculations assume that the metalloproteins are populated with iron. These iron use by metabolism estimates should be lower than total cellular iron due to use in other unconstrained iron reservoirs such as other metalloenzymes (e.g., aconitase), bacterioferritin storage, and chaperones. As a result, we use the terminology "iron-metalloenzyme inventory" to describe the total number of iron atoms that could be associated with each metabolism based on our measurements of peptide abundance.

Global Circulation Ecosystem Modeling. We used the global three-dimensional physical-biogeochemical-ecosystem model of Follows et al. (12) to investigate the potential global importance of hotbunking trophs. The model used here had various adaptations discussed in Dutkiewicz et al. (13) and Monteiro et al. (14), in particular to explicitly include nitrogen-fixing phytoplankton (diazotrophs) and a representation of denitrification. We use the Massachusetts Institute of Technology (MIT) general circulation model (MITgcm) and the physical circulation flow fields and diffusion are state estimates as produced by ECCO-GODAE and have been constrained by observations (15). The biogeochemical cycling of nitrogen, phosphorus, silicon and iron is represented and the ecosystem model includes several types of autotrophs consisting of nondiazotrophs and diazotrophs. The model re-

solves a diatom-analog, an analog of other large eukaryotes, high and low light *Prochlorococcus*-analogs, an analog of other small phytoplankton, *Trichodesmium*-analog, hotbunking unicellular diazotrophs (analogs of *Crocosphaera watsonii*) and nonhotbunking unicellular diazotrophs (a hypothetical control group). Non-diazotrophs' growth could be limited by phosphorus, silica (for diatoms), iron or nitrogen; diazotrophs growth is limited by phosphorus or iron. Growth rates are parameterized as a function of light, temperature and nutrient concentration. Simple allometric trade-offs are imposed (see refs. 12 and 13 for more discussion), in particular smaller phytoplankton have lower nutrient half-saturations (more efficient at acquiring nutrients) than large phytoplankton. The model also resolves explicit grazing and sinking and all organic and inorganic components were advected and diffused by the physical fields. Parameter values for the different phytoplankton analogs are taken from those found most fit in a previous simulation representing 10s of phytoplankton types (14). Here, given the number of simulations required, we only resolve the above 8 functional types. Additional modifications over (14) are to use the aeolian iron source fields as modeled by (16) that includes estimation of the variable solubility of the iron in seawater, as well as to include a sedimentary source of iron [following Elrod et al. (17)]. These modifications to the iron cycling parameterization used in Monterio et al. (14) provided more iron in some regions of the ocean (e.g., Equatorial Pacific) that had been potentially too low in Monterio et al., though this also leads to concentrations too high relative to observations in other regions (e.g., North Atlantic).

The hotbunking diazotrophs were modeled with a lower cellular iron to nitrogen ratio (R) relative to the control group as a consequence of their ability to share iron between photosynthesis and nitrogen fixation processes. But because this is an energetically expensive process, we also assumed that the hotbunking diazotrophs had a lower growth rate (μ) than the control group:

$$\mu_H = \alpha\mu_C, \qquad R_H = \gamma R_c \quad \text{where } \alpha,\gamma < 1.$$

The subscript H refers to the hotbunking group and C refers to the control nonhotbunking group. The trade-off between reduced growth and iron requirement is therefore represented by the values of α and γ. A larger value of α indicates less energetic cost, and a larger value of γ indicates iron requirements closer to the control group. We conduct several simulations with different combinations of α and γ. The laboratory studies described here suggest a decrease of iron requirement by as much as 40% ($\gamma = 0.6$), thus we consider a range of $\gamma = [0.5,0.6,0.7,0.8,0.9, 0.95]$. Crude back of the envelope calculations on the energetic cost suggest that it is at least 5%, but potentially several fold higher. Thus we consider the cost to growth $\alpha = [0.5,0.6,0.7,0.8, 0.9,0.95]$. Fig. 5 is constructed from results from the 36 simulations with the combinations of these values of α and γ. The simulations were run for 10 years and results from the annual mean for the tenth year are shown in Fig. 4 and Fig. S5. In all the experiments we set $\mu_C = 0.7\ \mathrm{d}^{-1}$, $K_{\mathrm{FeC}} = 0.36$ nM, and $R_C = 7.5 \times 10^{-4}$ mol Fe/mol N. We relate the change in the iron cellular demand (R) to the half saturation coefficient of growth (K_{Fe}) following Verdy et al. (18).

SI Results and Discussion

Global Proteome Results. Relative quantitation results obtained using 1D chromatography LC-MS analysis of the day-night experiment resulted in 477 unique protein and 3,800 unique tryptic peptides identifications with a false positive rate (FPR) of 0.65% (5), based on 20,506 total peptide identifications from 12 LC-MS injections (6 technical replicates per sample) and a total of 380,015 mass spectra (Dataset S1). Additional 2D chromatography analyses of the day-night experiment identified 1,108 unique proteins and 3,540 unique tryptic peptides (Dataset S1) for 18% coverage of the genome open reading frames and a 0.11% FPR, based on 21,620 total peptide identifications over 40 LC-MS fraction injections (~20 fractions per sample) for a total of 388,076 mass spectra. The diel experiment and iron stress experiments also identified 552 and 589 proteins, respectively, for a combined total of 724 proteins identified from the 1D global proteome experiments (day-night, diel, and iron stress experiments, see Dataset S1 for complete list of protein identifications, spectral count values of technical replicates, and fold change calculations). As is typical of proteomic experiments, each individual injection provided a large number of protein identifications, whereas repeat injections and 2D chromatographic separation provided confidence in the robustness of the results and increased proteome coverage incrementally with discovery of lower abundance tryptic peptides.

Examination of Flavodoxin and Ferredoxin Expression by Iron Stress Experiment. Whereas ferredoxin and flavodoxin are typically involved in electron transport in photosynthesis, an electron donor is also needed for the nitrogenase enzyme in the diazotrophic cyanobacterial species. Ferredoxins contain iron-sulfur centers and have a higher catalytic efficiency than the iron-free flavodoxin (19). In marine phytoplankton flavodoxin is generally considered a low-iron alternative to ferredoxin that is upregulated under iron stress in eukaryotic algae. Based on this expression behavior, flavodoxin has been applied as an iron nutrition diagnostic (20). Yet, as described in the main text, the expression of flavodoxin in *Crocosphaera* diverged from this behavior and was clearly present and abundant at night in *Crocosphaera* under iron-replete conditions (Fig. 3*D*).

The effect of reduced iron availability on the flavodoxin expression in the *Crocosphaera* proteome was examined through the growth of cultures under high and low total iron concentration, as well as with and without the addition of the strong iron chelator desferrioxamine B (DFB; Fig. S1 *C–F*). Cell counts showed a cessation of growth with the addition of DFB in both iron conditions, whereas the no iron added treatment did not show a physiological effect, as evidenced by growth similar to that of the standard (+Fe) media. This similar growth was expected based on the lack of multiple transfers in low-iron media, and allowed a low-iron treatment under similar growth rates for comparison with the replete iron. DFB is an exogenous siderophore and is known to greatly reduce the iron available to phytoplankton by depressing the abundances of the free ionic form and inorganic chemical species of the metal (21, 22). Flavodoxin protein expression under iron stress was examined during the light period because the influence of iron stress would potentially be difficult to differentiate from the high dark period expression observed (Fig. 3*D*). Flavodoxin (Cwat4291) was more abundant under high iron relative to no iron added (Fig. S1*D*), although both of these light period treatments were >5-fold less than the large peak in flavodoxin observed during the dark period in the day-night experiment (Fig. S2 and Fig. 1*B* in spectral count units; also Fig. 3*D*). Flavodoxin during the day period did not appear affected by DFB. Additionally, ferredoxin (Cwat3830) was 3-fold more abundant under high iron conditions relative to low-iron conditions (Fig. S1*D*), regardless of whether DFB was added. The absence of a light period increase in flavodoxin abundance under these two iron stress treatments (−Fe, and +DFB) suggests that flavodoxin's primary role is as the major electron donor protein for nitrogen fixation, rather than as a low-iron substitute for ferredoxin associated with photosynthesis as observed in other phytoplankton (19, 20, 23). The dark period expression of flavodoxin even under iron-replete conditions may be an adaptation for the minimization of *Crocosphaera*'s cellular iron demand.

Analysis of other putative ferredoxins in the genome revealed that three ferredoxin-like proteins lack more than one suitable

tryptic peptide for shotgun mass spectrometry detection. Because confidence in protein identification increases greatly with the identification of more than one tryptic peptide for a given protein, some of these small putative ferredoxin proteins may have been present but were not detected. Many open reading frames are annotated as ferredoxin in the current *Crocosphaera watsonii* genome, but of these only four were identified in our proteome samples. Cwat3830 is a 2Fe-2S ferredoxin, whereas Cwat5974 is misannotated and is actually *psaC*. Cwat5441 and Cwat1598 are barely detected and are likely too large to be real ferredoxins. We suspect that due to the small size of this protein, the major cellular ferredoxin has gone undetected in our study due to the lack of a suitable tryptic peptide within the sequence. Cwat1273, Cwat1274, and Cwat0916 are possible candidates for the major ferredoxin because all are lacking more than one suitable internal tryptic peptide needed for the shotgun proteomic techniques applied here.

Several other notable changes in global protein expression under iron stress were observed as shown in Fig. S1 *E* and *F* and Dataset S1, including a tripling in relative abundance of a possible carbon concentrating mechanism/microcompartments protein (Cwat5294) under low-iron without the addition of DFB. Ribulose-bisphosphate carboxylase (Cwat2714) was two to three-fold more highly expressed under low-iron, and fructose-bisphosphate aldolase (Cwat1319), which is involved in carbohydrate synthesis, was 20-fold higher under iron stress. The upregulation of these proteins suggests that reduced iron availability results in cellular demand for more efficient inorganic carbon fixation. *Crocosphaera* strains have been observed to secrete significant amounts of extracellular organic material (24). The increases in carbon fixation proteins under iron stress observed here may be connected to these organic secretions, perhaps to promote bacterial associations that produce siderophores and aid iron scavenging and acquisition (25).

Other Proteins of Interest. Cytochrome c550 is a monoheme cytochrome containing 1 Fe atom present as a component of the PSII complex of cyanobacteria and involved in the stabilization of the PSII Mn cluster (26). It has also been isolated as a soluble protein with a possible additional role in anaerobic carbon and hydrogen metabolism (11). This protein had a particularly strong diel pattern decreasing 15-fold during the dark from the daytime maximum as measured by targeted proteomic analysis (Fig. 3*G*). This decreased abundance during the dark period should reduce the oxygen production capability of PS II, which would be beneficial to the preventing damage to the nitrogenase complex. Cytochrome b6 also decreases in abundance by more than 2-fold during the dark period in our targeted proteomic analyses (Fig. 3*H*). This protein is a component of the b6f complex, which contains four iron containing heme groups and an Fe_2S_2 cluster (27) and is reported to have a dual function in photosynthesis and respiration in cyanobacteria (28).

Two heme oxygenases (Cwat4859, Cwat2459) were identified in the proteome, one with a dark period maxima (Cwat2459) and the other with a day period maxima (Cwat4859) in relative abundance (Fig. S2). Heme oxygenases are capable of releasing iron from hemes, for example by pathogenic bacteria to gain nutritional iron from host cells (29). This enzyme has also been shown to be involved in phycobilin synthesis in cyanobacteria through the conversion of hemin to ferric-biliverdin IX_{α},(29). We hypothesize that one of these heme oxygenases (Cwat2459) is involved in releasing the iron from cytochrome heme groups at night for use in the nitrogenase complex, whereas the other (Cwat4859) is involved in the conversion of hemin to ferric biliberdin IX_{α} phycobilin. Peptidase S41A also showed strong diel cycling with a presence during the photoperiod (Fig. S2), suggestive of its involvement in the changing proteome composition throughout the diel cycle (e.g., Fig. 2). Measurements of the ribosomal protein L3 (Cwat2439) are consistent with two more highly active periods of protein synthesis per diel cycle (Fig. S3*C*), and is consistent with the two peaks of ribosomal protein activity observed in the diel global proteome in Fig. 2. Plastocyanin, the copper containing water soluble electron carrier, was identified in the *Crocosphaera* proteome (Dataset S1). In addition, the iron-manganese superoxide dismutase present in the genome (Cwat6299) was not found in any of the proteome analyses here, whereas a nickel superoxide dismutase was detected in the 2D proteome (Cwat2983; Dataset S1), consistent with the theme of iron conservation in *Crocosphaera*.

Connecting Cellular Iron Estimates with Iron Biogeochemistry, Uptake, and Cell Division. Cellular iron was estimated during a diel cycle by combining light period ferrous iron uptake (30), our proteomic measurements, and allowing cell division after dawn. As mentioned in the main text, the motivation for this effort was to reconcile our diel protein cycling observations with the observation of increased cellular iron during the dark period in Tuit et al's study (31) by overlaying the two processes of cell division and ferrous iron uptake (and their temporal variability) onto our iron-metalloenzyme inventories. Before describing the results of this calculation below, we describe what is known about each of these processes with respect to *Crocosphaera*.

Cell division is known to occur solely during the photoperiod in *Crocosphaera* (e.g., Fig. S3*A*), and division must divide the cellular iron between two daughter cells, perhaps also involving some cellular leakage in the process. With growth rates of $\sim$0.5 d^{-1} observed in Tuit et al. (31), 65% of cells are dividing daily, contributing to a 40% decrease in iron per cell when averaged across the population. Hence, cell division alone can account for a significant amount of the lower photoperiod cellular iron content observed by Tuit et al. In addition, a potential iron uptake pathway for *Crocosphaera* involves a combination of photochemical reduction of the natural iron ligands that dominate seawater iron chemistry or Fe–EDTA complexes in laboratory media and uptake of the resultant ferrous iron (30, 32, 33). This scenario would cause production of Fe(II) during the light period followed by rapid reoxidation and complexation by strong ligands in darkness at tropical and subtropical temperatures as modeled by Weber et al. (30) (Fig. S4*A*). In addition, the *Crocosphaera watsonii* genome contains genes for the ferrous iron transporter, which a recent microarray transcriptional study showed are greatly upregulated during the photoperiod (34), consistent with light period photochemical ferrous iron source. Ferrous iron is very rapidly oxidized to ferric iron in seawater (35), and hence only exists in appreciable amounts during the photoperiod under the tropical temperature conditions of *Crocosphaera*'s niche (30). *Crocosphaera*'s genome does not appear to contain genes for other important iron acquisition mechanisms such as an iron reductase system, siderophore biosynthesis, or siderophore transport (36). These facts taken together suggest a scenario where *Crocosphaera* acquires ferrous iron during the light period, resulting in iron accumulating through the light period as shown in the schematic in Figs. S4 *A* and *B*.

Combining the influence of the temporal processes of cell division and ferrous iron uptake, with our diel iron-metalloenzyme inventory calculations allows a schematic of diel cellular iron budget to be estimated that might be expected in natural environments. Ferrous iron uptake was calculated to be proportional to the light period ferrous iron availability from Weber et al. (30) (Fig. S4*A*), where the timing of iron uptake was inferred from chemical modeling of ferrous iron abundance (30), whereas the magnitude of uptake was tuned to minimize storage category (see below) to emphasize the extent of intracellular trafficking and to allow a steady-state cellular iron abundance. The iron estimated to be involved in nitrogen fixation and photosynthesis (Fig. 3 *I* and *J*) was then subtracted to make a rough estimate of

the remaining cellular iron that might be found in storage (bacterioferritin), other enzymes (e.g., aconitase), and chaperones (storage category from hereon). This storage/other reservoir is estimated to be quite dynamic during the diel cycle as shown in red in Fig. S4*B*. No efflux term is needed in these calculations to approximate steady-state growth. Increasing the ferrous iron production and resultant uptake rate in this calculation increases this reservoir as well as cellular iron in subsequent generations, as might be expected during transient pulses caused by dust input or increased light fluxes, presumably with iron storage in bacterioferritin. Our estimates of cellular iron associated with iron metalloenzymes involved in photosynthesis and nitrogen fixation are consistent with previous quota studies (10, 31, 37) differing by a factor of less than 2, which is within the error observed in those cellular iron measurements. This schematic also highlights the possibility of apo forms of nitrogen fixation and photosynthetic metalloenzymes existing, a likely scenario given the challenge of coordinating the movement of iron between intracellular reservoirs as estimated here. Future research on how chaperones and metal trafficking are involved in the diel metalloenzyme cycling we have observed would be particularly interesting in *Crocosphaera watsonii*.

Global Circulation Ecosystem Modeling. The simulations produced nutrient and biomass fields that compare well with observations. Total global primary production was between 38.2 and 38.8 GtC/y and total global nitrogen fixation rates were between 90 and 107 TgN/y (depending on the values of α and γ). The distribution of the different phytoplankton types compare well to observations, as shown in Follows et al. (12), Dutkiewicz et al. (13) and Monteiro et al. (14). Though never dominant in the model, diazotrophs could coexist with nondiazotrophs in regions where nitrate concentrations are low and there is sufficient iron and phosphorus for the diazotrophs to exist (38). Unicellular diazotrophs, due to their small size, can out-compete the *Trichodesmium*-analogs in more oligotrophic regions and their distribution and abundance are broadly consistent with those suggested by observations (14, 39). Observations of *Crocosphaera* as summarized in ref. 14 suggest higher abundances in the tropical North Atlantic (40, 41), eastern subtropical North Pacific (42, 43) and Arabian Sea (44). *Crocosphaera* have also been detected in the eastern subtropical North Atlantic (40) and eastern tropical South Atlantic (41), eastern subtropical and tropical North Pacific (42) and western South Pacific (45). They were however not detected in the western subtropical North Atlantic (40), eastern subarctic North Pacific, and eastern subtropical South Pacific (46). The pattern of presence and absence of *Crocosphaera*-analogs is in general captured by the numerical model (Fig. 4), with concentration levels consistent in most regions with the observations (see ref. 14 for details). The iron concentrations in the Caribbean and eastern tropical North Atlantic are too high in this version of the model, leading to strong phosphorous limitation there. This discrepancy leads to less than ideal conditions for diazotrophs, and concentrations there do not compare as well as in other parts of the oceans. A similar problem was found by Moore et al. (47). Presence, absence and abundances of *Trichodesmium*-analogs are also, in general, captured by the model. In particular the geographic patterns of *Trichodesmium* limited to regions with higher iron and *Crocosphaera* existing in regions with lower iron matches patterns suggested by the observations of Campbell et al. (45), who found that in the southwest Pacific *Trichodesmium* appeared constrained to coastal areas with high iron, whereas *Crocosphaera* dominated in offshore waters where Fe was low.

A series of experiments were conducted with varying degrees of trade-off between cellular iron to nitrogen reduction (γ) and cost to growth rate (α). These results (Fig. 5) indicate that the cost to growth cannot be too high (small α) or the hotbunkers do not survive. However, for lower cost to growth, hotbunking can confer an advantage in low-iron regions (Fig. 4 and Fig. S5). With the right combinations of α and γ the hotbunking diazotrophs could inhabit some model regions that would not support the control group (Fig. S5 *B* and *D*): The maximum area covered by unicellular diazotrophs increases by over 30% (from 59×10^6 km^2 to more than 79×10^6 km^2; Fig. 5 *A* and *B*) from simulations where only the control group survived to ones where hotbunkers are the only unicellular group surviving. However, the region of parameter space (α, γ) where hotbunkers completely out-compete the control group (white area of Fig. 5*B*) is quite small, suggesting that the energetic cost cannot be too high and there must be a significant reduction in iron needs. With more advantageous values of α and γ, the hotbunking diazotrophs could even outcompete *Trichodesmium* in some specific areas of the model ocean, leading to a reduced global biomass of *Trichodesmium* in those simulations (compare Fig. 4*A* and Fig. S5 *A* and *B*).

The value of γ also affected the local concentration of hotbunking diazotrophs. Simulations with lower requirement for iron (γ smaller) leads to a larger biomass of unicellular diazotrophs at any location compared to simulations with higher γ: the same iron supply could support a higher biomass. This leads to a globally increased biomass of hotbunking unicellular diazotrophs (Fig. 5*C*) with lower γ, and consequently an increase in total global nitrogen fixation (Fig. 5*D*) by as much as 20% (from 90 GtN/y for simulations with no hotbunkers to 107 GtN/y for most extreme case of α and γ, bottom right Fig. 5*D*). We note that more reasonable values of the trade-off would suggest a 5 to 10% increase. Because over many regions of the ocean the nondiazotrophic phytoplankton are nitrogen limited, this increased source of fixed nitrogen led to increased primary production. Globally this increase was as much as 1.5% between a simulation with no hotbunking unicellular diazotrophs (poor combination of α and γ) and one where hotbunkers outcompeted the control group everywhere (advantageous α and γ).

Other Supporting Information Files

Dataset S1 (XLSX)

1. Waterbury JB, Willey JM (1988) Isolation and growth of marine planktonic cyanobacteria. *Methods of Enzymology* eds Packer L, Glazer AN (Academic, San Diego), pp 100–105.
2. Saito MA, Moffett JW, Chisholm SW, Waterbury JB (2002) Cobalt limitation and uptake in *Prochlorococcus*. *Limnol Oceanogr* 47:1629–1636.
3. Ernst A, Kirschenlohr H, Diez J, Boger P (1984) Glycogen content and nitrogenase activity in *Anabaena variabilis*. *Arch Microbiol* 140:120–125.
4. Keller A, Nesvizhskii AI, Kolker E, Aebersold R (2002) Empirical statistical model to estimate the accuracy of peptide identifications made by MS/MS and database search. *Anal Chem* 74:5383–5392.
5. Peng J, Elias JE, Thoreen CC, Licklider LJ, Gygi SP (2003) Evaluation of multidimensional chromatography coupled with tandem mass spectrometry (LC/LC-MS/MS) for large-scale protein analysis: The yeast proteome. *J Proteome Res* 2:43–50.
6. de Hoon MJL, Imoto S, Nolan J, Miyano S (2004) Open source clustering software. *Bioinformatics* 20:1453–1454.
7. Eisen MB, Spellman PT, Brown PO, Botstein D (1998) Cluster analysis and display of genome-wide expression patterns. *Proc Natl Acad Sci USA* 95:14863–14868.
8. Stemmann O, Zou H, Gerber SA, Gygi SP, Kirschner MW (2001) Dual inhibition of sister chromatid separation at metaphase. *Cell* 107:715–726.
9. Raven JA (1988) The iron and molybdenum use efficiencies of plant growth with different energy, carbon and nitrogen sources. *Plant Phytol* 109:279–287.
10. Kustka A, Sanudo-Wilhelmy S, Carpenter EJ, Capone DG, Raven JA (2003) A revised estimate of the iron use efficiency of nitrogen fixation, with special reference to the marine cyanobacterium *Trichodesmium* spp. (Cyanophyta). *J Phycol* 39:12–25.
11. Krogmann DW (1991) The low-potential cytochrome c of cyanobacteria and algae. *Biochim Biophys Acta* 1058:35–37.
12. Follows MJ, Dutkiewicz S, Grant S, Chisholm SW (2007) Emergent biogeography of microbial communities in a model ocean. *Science* 315:1843–1846.
13. Dutkiewicz S, Follows MJ, Bragg J (2009) Modelling the coupling of ocean ecology and biogeochemistry. *Global Biogeochem Cy* 23:GB4017.
14. Monteiro F, M.J. Follows, & Dutkiewicz S (2010) Distribution of diverse diverse nitrogen fixers in the global ocean. *Global Biogeochemical Cycles* 24:10.1029/2009GB003731.

15. Wunsch C, Heimbach P (2006) Estimated decadal changes in the North Atlantic meridional overturning circulation and heat flux 1993–2004. *J Phys Oceanogr* 36:2012–2024.
16. Luo C, et al. (2008) Combustion iron distribution and deposition. *Global Biogeochemical Cycles* 22:10.1029/2007GB002964.
17. Elrod VA, Berelson WM, Coale KH, Johnson K (2004) The flux of iron from continental shelf sediments: A missing source for global budgets. *Geophys Res Lett* 31:10.1029/2004GL020216.
18. Verdy A, Follows M, Flierl G (2009) Evolution of phytoplankton cell size in an allometric model. *Mar Ecol-Prog Ser* 379:1–12.
19. Raven JA, Evans MCW, Korb RE (1999) The role of trace metals in photosynthetic electron tranpsort in O_2-evolving organisms. *Photosynth Res* 60:111–149.
20. LaRoche J, Boyd PW, McKay RML, Geider RJ (1996) Flavodoxin as an in situ marker for iron stress in phytoplankton. *Nature* 382:802–805.
21. Wells ML (1999) Manipulating iron availability in nearshore waters. *Limnol Oceanogr* 44:1002–1008.
22. Hutchins DA, Franck M, Brezezinski MA, Bruland KW (1999) Inducing phytoplankton iron limitation in iron-replete coastal waters witha a strong chelating ligand. *Limnol Oceanogr* 44:1009–1018.
23. Erdner DL, Anderson DM (1999) Ferredoxin and flavodoxin as biochemical indicators of iron limitation during open-ocean iron enrichment *Limnol Oceanogr* 44:1609–1615.
24. Webb EA, Ehrenreich IM, Brown SL, Valois FW, Waterbury JB (2009) Phenotypic and genotypic characterization of multiple strains of the diazotrophic cyanobacterium, *Crocosphaera watsonii*, isolated from the open ocean. *Environ Microbiol* 11:338–348.
25. Amin SA, et al. (2009) Photolysis of iron siderophore chelates promotes bacterial algal mutualism. *Proc Natl Acad Sci USA* 106:17071–17076.
26. Kerfeld CA, et al. (2003) Structural and EPR characterization of the soluble form of cytochrome c-550 and of the psbV2 gene product from the cyanobacterium *Thermosynechococcus elongatus*. *Plant Cell Physiol* 44:697–706.
27. Kurisu G, Zhang H, Smith JL, Cramer WA (2003) Structure of the cytochrome b6f complex of oxygenic photosynthesis: Tuning the cavity. *Science* 302:1009–1014.
28. Peschek GA, Schmetterer G (1982) Evidence for plastoquinol-cytochrome f/b-563 reductase as a common electron donor to P700 and cytochrome oxidase in cyanobacteria. *Biochem Bioph Res Co* 108:1188–1195.
29. Migita CT, Zhang X, Yoshida T (2003) Expression and characterization of cyanobacterium heme oxygenase, a key enzyme in the phycobilin synthesis. *Eur J Biochem* 270:687–698.
30. Weber L, C.Volker, Oschlies A, Burchard H (2007) Iron profiles and speciation of the upper water column at the Bermuda Atlantic time-series study site: a model based sensitivity study. *Biogeosciences* 4:689–706.
31. Tuit C, Waterbury J, Ravizza G (2004) Diel variation of molybdenum and iron in marine diazotrophic cyanobacteria. *Limnol Oceanogr* 49:978–990.
32. Voelker B, Morel FMM, Sulzberger B (1997) Iron redox cycling in surface waters: Effects of humic substances and light. *Environ Sci Technol* 31:1004–1011.
33. Shaked Y, Kustka AB, Morel FMM (2005) A general kinetic model for iron acquisition by eukaryotic phytoplankton. *Limnol Oceanogr* 50:872–882.
34. Shi T, Ilikchyan I, Rabouille S, Zehr JP (2010) Genome-wide analysis of diel gene expression in the unicellular N_2-fixing cyanobacterium *Crocosphaera watsonii* WH 8501. *ISME J* 4:621–632.
35. Millero FJ, Sotolongo S, Izaguirre M (1987) The oxidation kinetics of Fe(II) in seawater. *Mar Chem* 51:793–801.
36. Hopkinson B, Morel FMM (2009) The role of siderophores in iron acquisition by photosynthetic marine microorganisms. *Biometals* 22:659–669.
37. Fu F-X, et al. (2008) Interactions between changing pCO_2, N_2 fixation, and Fe limitation in the marine unicellular cyanobacterium *Crocosphaera*. *Limnol Oceanogr* 53:2472–2484.
38. Monteiro F, Dutkiewicz S, Follows MJ (2010) Biogeographical controls on marine nitrogen fixers. *Global Biogeochemical Cycles* 10.1029/2010GB003902.
39. Moisander PH, et al. (2010) Unicellular cyanobacterial distributions broaded the oceanic N_2 fixation domain. *Science* 327:1512–1514.
40. Langlois RJ, Hummer D, LaRoche J (2008) Abundances and distributions of the dominant nifH phylotypes in the northern Atlantic ocean. *Appl Environ Microb* 74:1922–1931.
41. Foster RA, Subramaniam A, Zehr JP (2009) Distribution and activity of diazotrophs in the eastern equatorial Atlantic. *Environ Microbiol* 11:741–750.
42. Church MJ, Björkman KM, Karl DM, Saito MA, Zehr JP (2008) Regional distributions of nitrogen-fixing bacteria in the Pacific Ocean. *Limnol Oceanogr* 53:63–77.
43. Church MJ, Short CM, Jenkins BD, Karl DM, Zehr JP (2005) Temporal patterns of nitrogenase gene (nifH) expression in the oligotrophic north Pacific ocean. *Appl Environ Microbiol* 71:5362–5370.
44. Mazard SL, Fuller NJ, Orcutt KM, Bridle O, Scanlan DJ (2004) PCR analysis of the distribution of unicellular cyanobacterial diazotrophs in the Arabian Sea. *Appl Environ Microbiol* 70:7355–7364.
45. Campbell L, Carpenter EJ, Montoya JP, Kustka AB, Capone DG (2005) Picoplankton community structure within and outside a *Trichodesmium* bloom in the southwestern Pacific Ocean. *Vie Milieu* 55:185–195.
46. Bonnet S, et al. (2008) Nutrient limitation of primary production in the Southeast Pacific (BIOSOPE cruise). *Biogeosciences* 5:215–225.
47. Moore JK, Doney SC, Lindsay K (2004) Upper ocean ecosystem dynamics and iron cycling in a global three-dimensional model. *Global Biogeochem Cy* 18:10.1029/2004GB002220.

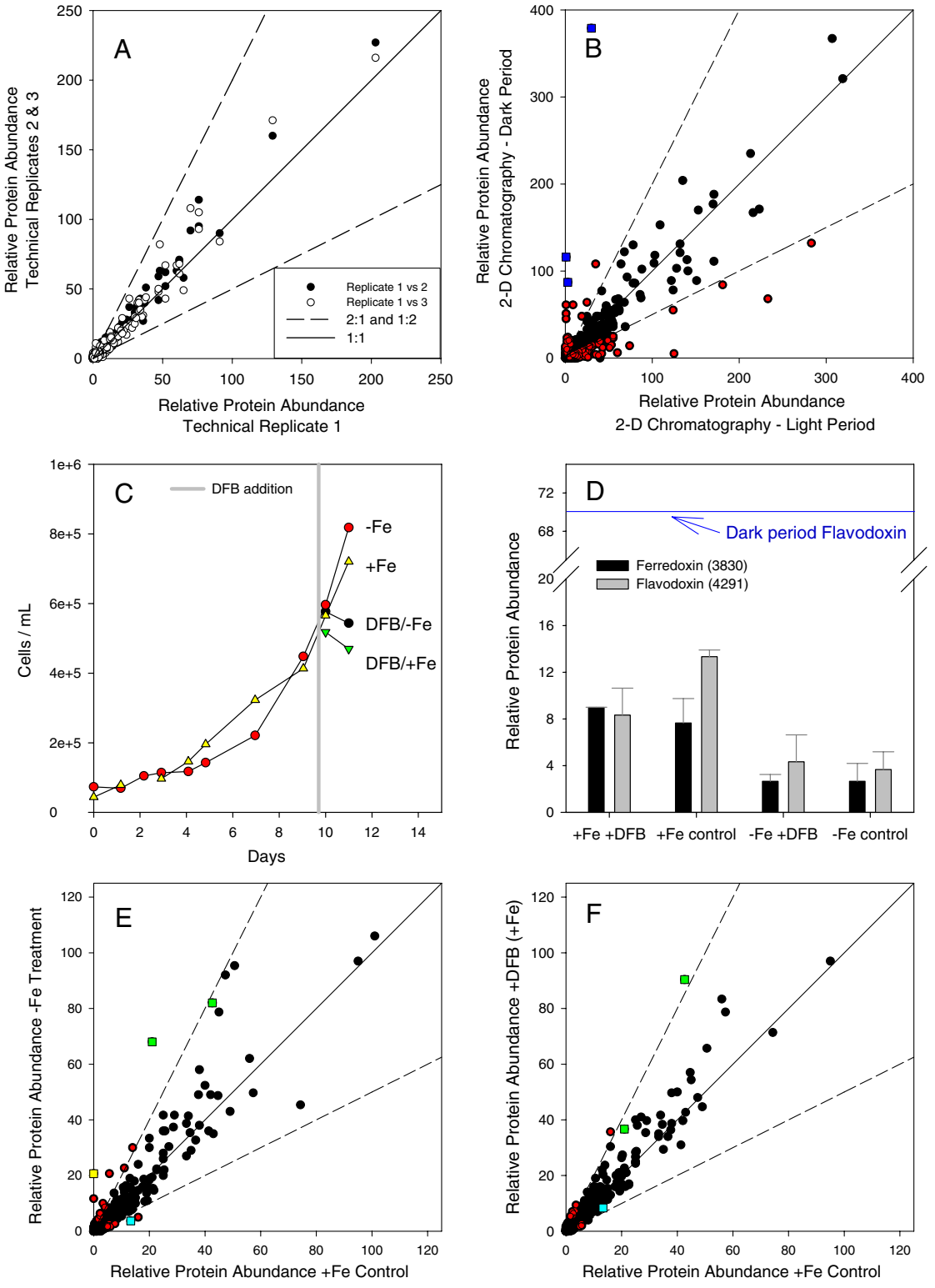

Fig. S1. Supplementary global proteome results. Relative protein abundance determined by spectral counting. (*A*) Comparison of three technical replicates from the light period from the light-dark experiment (Fig. 1*B*) showed good reproducibility; 1:1 and 2-fold change lines are shown for comparison. (*B*) Comparative global proteomes of the light-dark experiment *Crocosphaera watsonii* samples as analyzed by 2D-chromatography. Proteins with greater than two-fold change in relative abundance are in red (≥5 spectral counts), with the exception of the nitrogenase metalloenzymes in blue squares; and trends are consistent with the 1D chromatography analyses in Fig. 1*B*. (*C*) Cell abundances during the iron stress experiment, where high and low abundance iron cultures were both split and one bottle of each was treated with 500 nM of the iron chelator DFB. Both DFB treatments showed cessation of growth within 24 h. (*D*) Relative abundance of ferredoxin and flavodoxin proteins in the iron stress experiment showed no increase in flavodoxin during the light period either under DFB addition or no iron added treatment, in contrast to the large dark period flavodoxin relative and absolute abundances observed in all dark period analyses (Figs. 1*B*, 2, and 3*D*; and Fig. S2). A decrease in ferredoxin (Cwat3830) was observed in treatments without added iron. Data and error bars are the average and standard deviation of technical triplicate analyses. (*E* and *F*) Comparative global proteomes of iron stress in *Crocosphaera* samples, with relative protein abun-

dance given by average of technical triplicate spectral counts from samples taken during growth in the light period under high and low-iron (*E*) and under high iron with and without the addition of iron chelator desferrioxamine B (*F*). Proteins with greater than 2-fold change (dashed lines) in relative abundance are in red (≥5 spectral counts). The carbon concentrating mechanism/microcompartments protein (Cwat5294) and ribulose-biphosphate carboxylase (Cwat2714), shown in green squares, appear modestly more abundant in iron limited treatments. Fructose-bisphosphate aldolase shown in yellow squares (panel *E*; Cwat2319) is involved in carbohydrate synthesis and was more abundant in low-iron. Flavodoxin shown in cyan squares (panels *E* and *F*; Cwat4291).

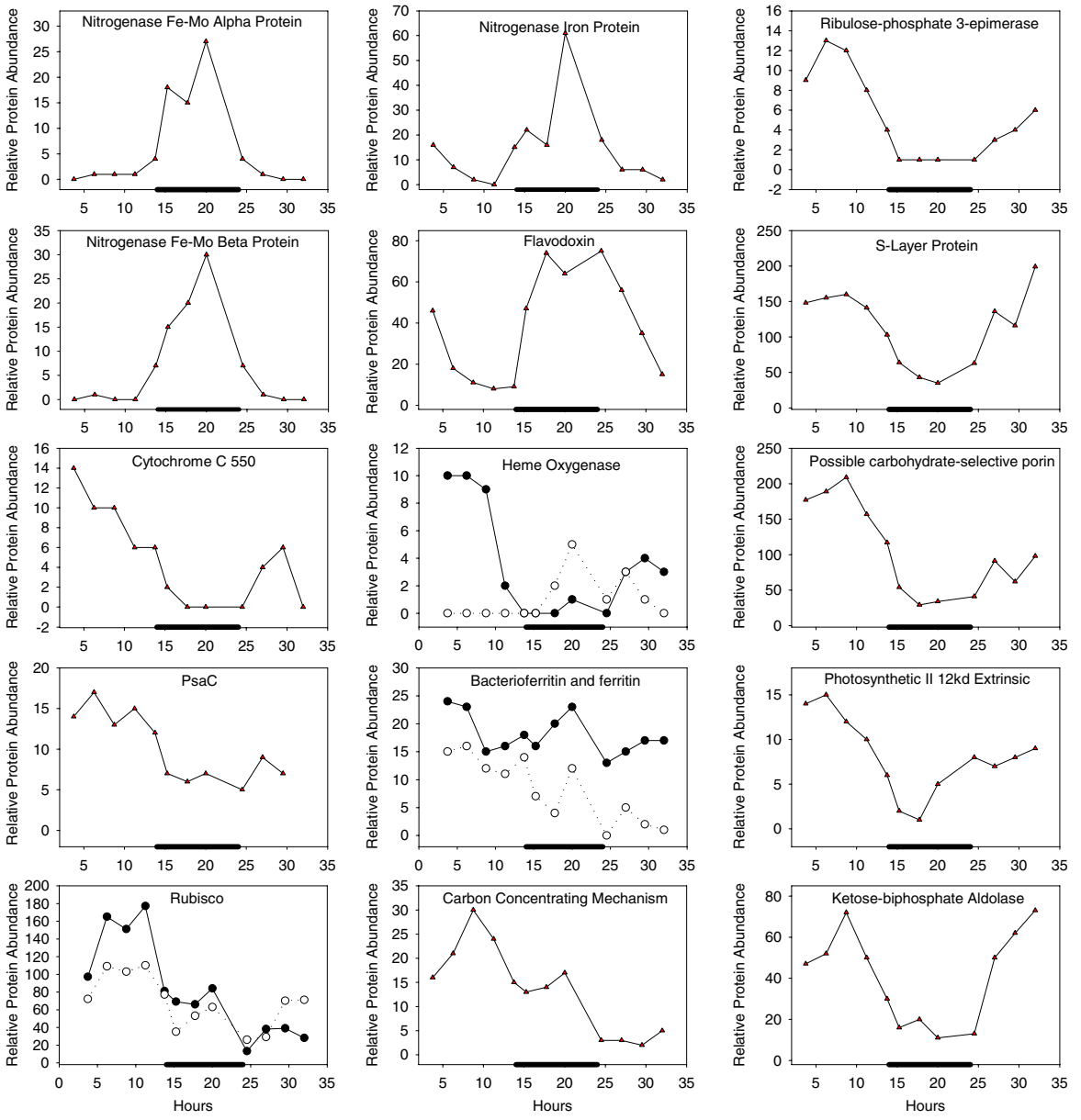

Fig. S2. Relative abundance of proteins of interest as determined using spectral counting. Relative abundance as determined by spectral counting on a linear trap mass spectrometer during the diel cycle (dark, black bar) showed good agreement with trends observed using targeted proteomic analysis on a triple quadrapole mass spectrometer for iron metalloproteins (Fig. 3). For the heme oxygenases, the empty circles are Cwat2459 whereas the filled circles are Cwat4859. The nitrogenase iron protein is Cwat3818, molybdenum-iron protein subunits MoFe α, MoFe β are Cwat3819 and 3120, flavodoxin is Cwat4291, and c550 is Cwat5304. PsaC is Cwat5975, bacterioferritin (closed) and ferritin (open) are Cwat5989 and Cwat4924, Rubisco refers to ribulose-bisphosphate carboxylase long (Cwat2714, closed) and short (Cwat2716, open) chain. Carbon concentrating mechanism is Cwat5296, ribulose-phosphate 3-epimerase is Cwat4803, and possible carbohydrate-selective porin is Cwat6588. S-layer protein is Cwat4220, photosynthetic II 12 kD extrinsic is Cwat0626, and ketose-biphosphate aldolase is Cwat3318.

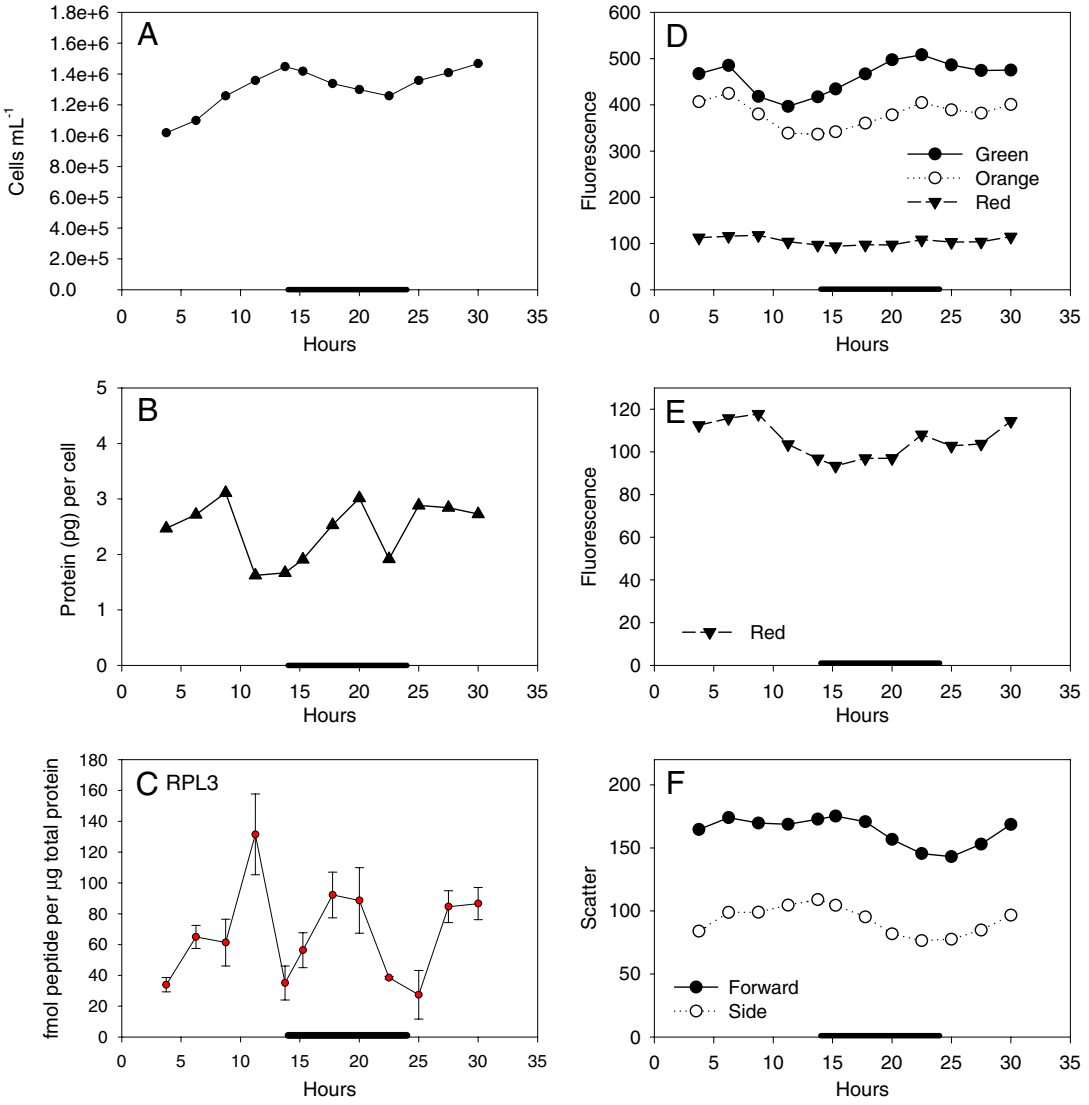

Fig. S3. Ancillary data for the diel *Crocosphaera* experiment. (*A*) Cell density at each time point, as measured by microscopy. (*B*) Total protein concentration in cellular extracts. (*C*) Targeted protein abundance of the ribosomal protein (RP) L3 (Cwat2439, see Table S2), displaying a triple peak consistent with two active periods of protein synthesis per diel cycle. (*D*) Fluorescence per cell as measured by flow cytometry, where green corresponds to a SYBR Green I DNA stain, orange for phycoerthyrin, and red for chlorophyll. (*E*) Expanded scale of red fluorescence per cell. (*F*) Forward and side scatter by flow cytometry with decreasing cell size at night as glycogen stores are consumed (see Fig. 1*A*).

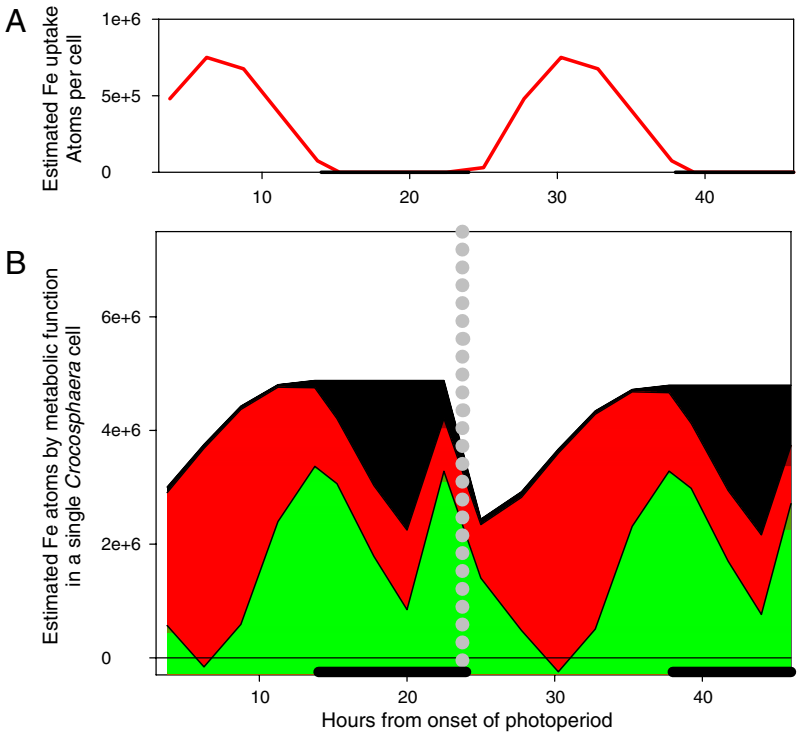

Fig. S4. Schematic of iron uptake and intracellular iron reservoirs in *Crocosphaera* during the diel cycle. (*A*) Idealized iron uptake during the light period (dark, black bar), where ferrous iron abundance has a midphotoperiod maximum due to photochemical reduction of abundant natural Fe(III)-ligand complexes and rapid abiotic reoxidation, consistent with chemical modeling (30), and ferrous iron is considered the accessible form of iron based on the presence of ferrous iron transporters (*feoA* and *feoB*) in the *Crocosphaera* genome. The magnitude of uptake was tuned to minimize the "other" category in steady-state (see below). (*B*) Estimated iron atoms used for nitrogen fixation (black), photosynthesis (red), and the aggregate of storage molecules (bacterioferritin), chaperones, and other metabolic functions (green; estimated by difference of total iron from uptake in (*A*) with the measured nitrogen fixation and photosynthesis reservoirs in Fig. 3), with the assumption of no iron loss or efflux. Cell division (dashed gray) halves the total iron inventory and each individual reservoir. This schematic shows that our measurements of iron metalloprotein inventories over the diel cycle, when combined with estimates of iron uptake and cell division, are consistent with observations of increases in iron quota in the dark relative to the light period (31).

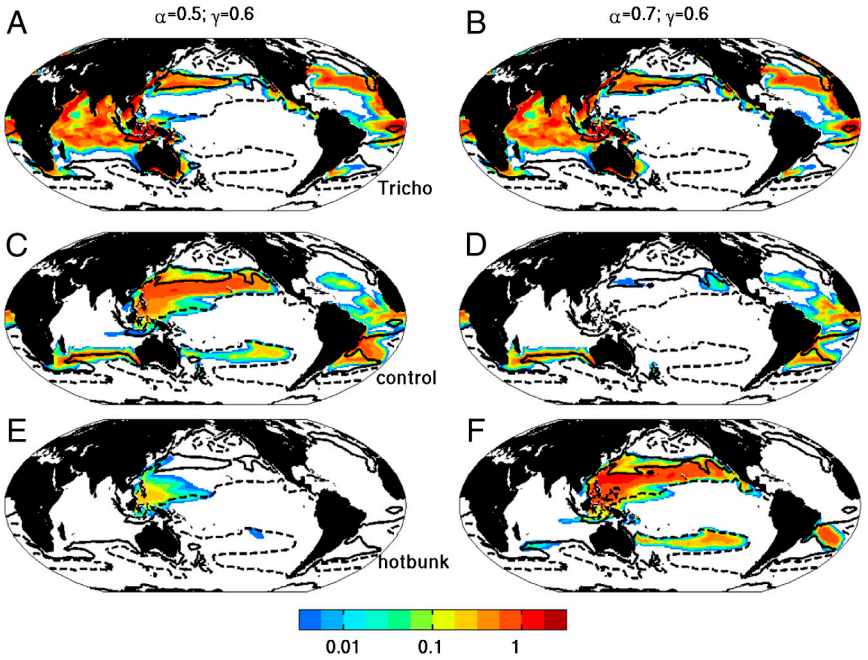

Fig. S5. Hotbunking unicellular diazotrophs habitat is determined by the assumption of the trade-off between lower iron requirement and energetic expense (values of γ and α). Left panels shows results from simulation where the energetic cost is assumed to be high ($\alpha = 0.5$, $\gamma = 0.6$, left cross in Fig. 5) and right panels where the energetic cost is lower ($\alpha = 0.7$, $\gamma = 0.6$, middle cross in Fig. 5). (*A*, *B*) Model analogs of *Trichodesmium*, (*C*, *D*) nonhotbunking unicellular diazotrophs (mgC m^{-3}), the control group; (*E*, *F*) hotbunking unicellular diazotrophs (mgC m^{-3}), analogs of *Crocosphaera watsonii*. Dashed and solid contours indicate 0.1 nM and 0.3 nM Fe respectively (see Fig. 4*A*), and no shading indicates areas devoid of unicellular diazotrophs. These results can be compared to a simulation with a lower energetic cost ($\alpha = 0.9$) shown in Fig. 4. With high cost (*Left*), hotbunking is not advantageous and the *Crocosphaera*-analogs are only competitive in regions where iron is very low (just enough to support diazotrophy). For more advantageous combination of α and γ (right panel), the hotbunking group will out-compete the control group in more regions, and with even higher α (Fig. 4), the hotbunking group will completely out-compete the control and their habitat will include waters with even lower iron supply (Fig. 4), and spread into regions inhabited by *Trichodesmium* simulations where the energetic cost was higher.

Table S1. Iron stoichiometry of photosynthesis and diazotrophy in cyanobacteria

Complex/protein	Iron content (reference)	Fe/complex or Fe/protein
Photosynthesis		
Photosystem I	3 Fe_4S_4 clusters (1)	12
Photosystem II	1 nonheme iron (1)	1
Cytochrome b-559	1 heme iron (1)	1
Cytochrome c-550	1 heme iron (2)	1
b_6f complex	4 heme, 1 Fe_2S_2 per monomer (3)	12 per dimer
Ferredoxin	2Fe-2S bacterial type (1)	2
Ferredoxin	4Fe-4S plant type (1)	4
Nitrogen fixation		
Nitrogenase	Fe protein (NifH) (4)	4 per homodimer
	MoFe protein (NifDK, α and β) (4)	15 per heterodimer
Flavodoxin	None (5)	0

1 Raven JA, Evans MCW, Korb RE (1999) The role of trace metals in photosynthetic electron transport in O_2-evolving organisms. *Photosynth Res* 60:111–149.
2 Kerfeld CA, et al. (2003) Structural and EPR characterization of the soluble form of cytochrome c-550 and of the psbV2 gene product from the cyanobacterium *Thermosynechococcus elongatus*. *Plant Cell Physiol* 44:697–706.
3 Kurisu G, Zhang H, Smith JL, Cramer WA (2003) Structure of the cytochrome b6f complex of oxygenic photosynthesis: Tuning the cavity. *Science* 302:1009–1014.
4 Rubio LM, Ludden PW (2008) Biosynthesis of the iron molybdenum cofactor of nitrogenase. *Annu Rev Microbiol* 62:93–111.
5 LaRoche J, Boyd PW, McKay RML, Geider RJ (1996) Flavodoxin as an in situ marker for iron stress in phytoplankton. *Nature* 382:802–805.

Table S2. Heavy and native sequences of peptides, their SRMs, and collision energies

Protein description	Peptide name	Peptide sequence	Parent m/z	Product m/z	Collision energy	Start time (min)	Stop time (min)
Photosystem 1 protein PsaB (Cwat 1223)	psaB L	TPLANLVR	442.272	501.314	18	12.9	15.1
				572.351	21	12.9	15.1
				685.436	21	12.9	15.1
	psaB H	TPLAN[L_C13N15]VR	445.78	508.331	18	12.9	15.1
				579.368	21	12.9	15.1
				692.452	21	12.9	15.1
Nitrogenase molybdenum-iron protein alpha subunit (Cwat3819)	MoFeA2 L	ILLEEIGLR	528.327	345.22	18	18	21
				716.39	19	18	21
				829.48	17	18	21
	MoFeA2 H	I[L_C13N15]LEEIGLR	531.84	345.22	18	18	21
				716.39	19	18	21
				829.48	17	18	21
Nitrogenase NifH protein (Cwat 3818)	nifH2 L	LNTQMIHFVPR	678.37	655.368	27	15.5	19
				768.452	23	15.5	19
				899.492	22	15.5	19
	nifH2 H	[L_C13N15]NTQMIHFVPR	681.88	655.37	27	15.5	19
				768.45	23	15.5	19
				899.49	22	15.5	19
Nitrogenase molybdenum-iron protein alpha subunit (Cwat 3819)	MoFeA1 L	LIADVLSTYPEK	674.872	373.208	29	15.2	17.6
				724.351	17	15.2	17.6
				837.435	20	15.2	17.6
				1122.567	21	15.2	17.6
	MoFeA1 H	[L_C13N15]IADVLSTYPEK	678.38	373.208	29	15.2	17.6
				724.351	17	15.2	17.6
				837.435	20	15.2	17.6
				1122.567	21	15.2	17.6
Cytochrome b6 of the b6f complex; PetB (Cwat 4239)	petB1 L	LEIQAISDDITTK	723.888	779.378	26	15.4	17.9
				892.462	28	15.4	17.9
				963.499	28	15.4	17.9
	petB1 H	[L_C13N15]EIQAISDDITTK	727.397	779.378	26	15.4	17.9
				892.462	28	15.4	17.9
				963.499	28	15.4	17.9
Photosystem 1 protein PsaA (Cwat 1222)	psaA1 L	VAVDVDPVPTSFEK	751.89	708.356	33	14.9	17.1
				904.477	27	14.9	17.1
				1019.504	24	14.9	17.1
	psaA1 H	VA[V_C13N15]DVDPVPTSFEK	754.897	708.356	33	14.9	17.1
				904.477	27	14.9	17.1
				1019.504	24	14.9	17.1
Flavodoxin, long chain, PetE (Cwat 4291)	petE1 L	FVGLPIDEINQSDK	787.907	591.273	32	16.7	19
				948.426	31	16.7	19
				1158.563	22	16.7	19
	petE1 H	FVG[L_C13N15]PIDEINQSDK	791.415	591.273	32	16.7	19
				948.426	31	16.7	19
				1158.563	22	16.7	19
Nitrogenase molybdenum-iron protein beta subunit (Cwat 3829)	MoFeB1 L	INFIPGFETYIGNLR	877.467	402.246	11	22.5	25.5
				459.267	20	22.5	25.5
				572.351	20	22.5	25.5
				836.462	8	22.5	25.5
				1266.648	30	22.5	25.5
				1379.732	20	22.5	25.5
	MoFeB1 H	INFIPGFETYIGN[L_C13N15]R	880.976	409.263	11	22.5	25.5
				466.285	20	22.5	25.5
				579.369	20	22.5	25.5
				843.479	8	22.5	25.5
				1273.664	30	22.5	25.5
				1386.749	20	22.5	25.5

Protein description	Peptide name	Peptide sequence	Parent m/z	Product m/z	Collision energy	Start time (min)	Stop time (min)
Photosystem II stabilizing cytochrome c550 (Cwat 5304)	c550 L	TNNNVSLGLEDLAGAEPR	935.469	529.272	35	16.6	19
				600.309	25	16.6	19
				1127.569	31	16.6	19
	c550 H	TNNNVS[L_C13N15] GLEDLAGAEPR	938.977	529.272	35	16.6	19
				600.309	25	16.6	19
				1127.569	31	16.6	19
Ribosomal protein L3 (Cwat 2439)	RPL3 L	TTETDGYSAVQLGYLEVK	987.489	708.392	31	16.8	19.2
				949.535	37	16.8	19.2
				1206.673	33	16.8	19.2
	RPL3 H	TTETDGYSAVQ[L_C13N15] GYLEVK	990.997	708.392	31	16.8	19.2
				956.552	37	16.8	19.2
				1213.689	33	16.8	19.2

List includes the proteins (description and Cwat number) selected for quantitative monitoring, the peptides, and their heavy labeled versions used as internal standards and the SRM transitions (parent and product ions), collision energies, and scheduled monitoring for triple quadropole mass spectrometery.